MODELING, SIMULATION, AND VALIDATION OF SINGLE PHOTON AVALANCHE DIODES FOR NV CENTER-BASED QUANTUM SENSING

Thesis

to obtain the degree of Bachelor of Science
at the Delft University of Technology,
to be defended publicly on Tuesday June 24, 2025 at 9:00 AM.

by

Isa SPOLER
Kevin VERMAAT

Student number:	Isa Spoler	5809886
	Kevin Vermaat	5705053
Project duration:	April 22, 2025 – June 24, 2025	
Thesis committee:	Prof. Dr. Ir. Leon Abelmann	TU Delft, jury chair
	Dr. S. Nur,	TU Delft, supervisor
	Dr. S. Izadkhast,	TU Delft

ABSTRACT

Nitrogen-Vacancy (NV) color centers in diamond are a promising and powerful technology for sensing small magnetic fields in the order of μT. One of its applications is the use in magnetic biosensing to identify cells marked with magnetic nanoparticles. These nanoparticles can target cells linked to malignant tissue, which can subsequently be identified with great spatial resolution using the NV centers. Therefore promising a less invasive procedure and more accurate identification. Such a system using NV centers as detectors requires small and effective photon detection hardware in order to be used in practice. In this bachelor graduation project Single Photon Avalanche Diodes (SPADs) are characterized, simulated and validated, to be integrated in a SPAD imaging sensor designed for magnetic bioimaging using NV centers.
A 3D model of the SPAD is created in TCAD Sentaurus to verify whether the designed SPAD performs as intended. To this end, the I-V and C-V curves are simulated. These graphs show that a proposed SPAD design works as intended whilst the previously implemented design does not. Furthermore, the simulation results can later be compared to the behavior of a physical SPAD. During the physical analysis of the stray SPADs on a previous IC, a design flaw was identified. To verify this a test circuit was built and the device was retested. The results confirm an error in the SPAD design. The SPAD is missing an N-well resulting in standard diode behavior and preventing it from detecting photons. Furthermore, to enhance single-photon detection, we explored a new analog-to-digital converter (ADC) circuit that employs a Schmitt trigger in place of a standard comparator. Our results show that this ADC delivers predictable behavior and achieves a more precise and efficient conversion to a digital signal.

PREFACE

The work presented in this thesis, titled Modeling, Simulation and Validation of Single Photon Avalanche Diodes for NV center-based Quantum Sensing, represents the culmination of our Bachelor's degree in Electrical Engineering at TU Delft. Over the course of this project, we refined our technical knowledge and developed new skills in semiconductor device design, circuit simulation, and experimental validation. We gained hands-on experience with TCAD modeling tools, advanced our understanding of quenching circuits and analog-to-digital conversion, and learned to navigate the challenges of translating theoretical concepts into functional hardware.
Throughout the project we have not only learned technical skills and acquired in depth knowledge concerning the topics discussed in this thesis, but we have also learned how to apply prior knowledge. With this we have gained a deeper understanding of what we have learned during each course in the bachelor and how to apply it.
We extend our deepest gratitude to our primary and daily supervisors respectively, Salahuddin Nur and Dylan Aliberti, for their support and guidance throughout this project. Additionally we would like to extend our gratitude to Ryoichi Ishihara, Diederik Dekkers and Nikolaj Nitzsche for attending our weekly meetings and their invaluable feedback. Lastly, we would like to express our sincere gratitude to our group members — Felix Barzilaij, Zhi Jin, Seppe Dijkstra, and Jurre Botman — for their support and invaluable input over the past two months. We truly couldn't have imagined sharing this journey with anyone else.

This thesis was carried out within the Quantum Integration Group (QIT) at Delft University of Technology, and we are thankful for the opportunity to contribute to this distinguished research group.

Isa Spoler
Kevin Vermaat
Delft, June 2025

CONTENTS

1
INTRODUCTION

Magnetic bioimaging using Nitrogen-Vacancy (NV) centers in diamond has been widely researched, yet a fully integrated system is still a long ways from being reality [1], [2]. Current systems are large and bulky and require multiple separate components to function and are still reliant on traditional methods for verification, such as fluorescent staining [2], [3]. In recent developments, Single Photon Avalanche Diodes (SPADs) are being implemented in arrays to create sensors for imaging instead of standard CMOS sensors, providing the ability to detect single photons as well as limiting background noise [4]. As such, a push for an integrated system which can be used for multiple different applications has begun.
In this thesis, the modeling and simulation of a singular SPAD device, will be discussed. Next, the validation of a previously fabricated SPAD will be laid out. Furthermore, the circuitry surrounding a SPAD to allow for the conversion of an analog signal to a digital signal will be analyzed and tested.

This chapter will discuss the problems that are addressed in and the context of this thesis. Additionally, background information regarding NV centers as well as SPADs and the basic circuitry surrounding one is given. Finally, a short synopsis of this thesis is given.

1.1. PROBLEM STATEMENT

In this section the context of this thesis and the problems addressed in this thesis will be discussed. First, the context of this project in the direction of magnetic bioimaging will be explained. Furthermore, the current state of SPAD imaging technology and the integrated system will be discussed. Afterwards, the SPAD sensor and its current limitations will be laid out.

1.1.1. MAGNETIC BIOIMAGING

Magnetic biosensing is already widely used in different applications, one of these being magnetic-activated cell sorting (MACS). For this, cells are marked using magnetic nanoparticles (MNPs) [5] and then sorted one by one into different containers dependent on how strongly magnetically marked they are [6]. This has the downside of requiring the cells to be suspended in liquid and moved around, as such the original location of the cells is unknown. Recently however, the advent of magnetic field sensing using NV centers has resulted in the possibility of determining the location of marked cells *in situ*, also called magnetic bioimaging [3]. The usage of NV centers allows for detection

of small magnetic fields in the order of μT originating from cells marked with MNPs [3]. Magnetic bioimaging is not a new technology, an example being the widely used MRI scans. However, these current techniques rely on bulky machines and lengthy procedures to get an accurate image.

One of the applications of magnetic bioimaging is the detection of cancerous cells, which is the focus of the research this project contributes to. Current techniques for determining the location of cancerous cells either require invasive techniques or lengthy procedures. Additionally, the sensitivity of current magnetic bioimaging techniques is limited. MRI scans still require multiple additional procedures, which are possibly very invasive, before a diagnosis can be made with utmost certainty [7], [8]. Magnetic bioimaging using NV centers has the potential of improving cancer detection by providing more precision in a device with a smaller form factor and lower usage costs, limiting the requirements for invasive procedures and improving the success rate of surgeries and improving patient wellness.

1.1.2. SPAD SENSOR

NV centers on their own cannot provide a full system for measurements. A secondary measurement system is required, either in the form of a CMOS camera sensor or an array of SPADs. Both of the options have their merits, especially with the level of development of current CMOS sensors. However, SPADs promise to deliver best in class performance for limiting background noise and detecting very low intensity optic signals [9]. Even so, there are currently some limitations concerning SPAD arrays and sensors; their resolution being the main limitation. Currently relatively few high resolution SPAD sensors are available, with focused efforts by Canon resulting in several megapixel camera sensors [4], [10], [11]. This shows that the technology has improved quite a lot and a SPAD sensor with high enough resolution specific for NV center readouts is possible, but as of yet still theoretical.

To be able to create such a SPAD sensor specifically for NV center readouts, integrating the diamond containing the NV centers onto the IC, requires multiple iterative design steps, including validation and verification of the device. A general overview of the full system focused on magnetic bioimaging can be seen in Fig. 1.1. The ultimate goal being the integration of The NV center and SPAD sensor layers into one.
The current SPAD imaging IC and other previous SPAD testing chips designed by the Quantum Integration Technology group[1] did not work as expected [12], [13]. It has been found that validation of the device prior to manufacturing has not been done, reflected in point 1 in Fig. 1.1. This and further optimisation of the circuitry surrounding the SPAD should provide further improvement to the SPAD sensor for NV center readout.

[1] QIT / Ishihara lab, Delft University of Technology

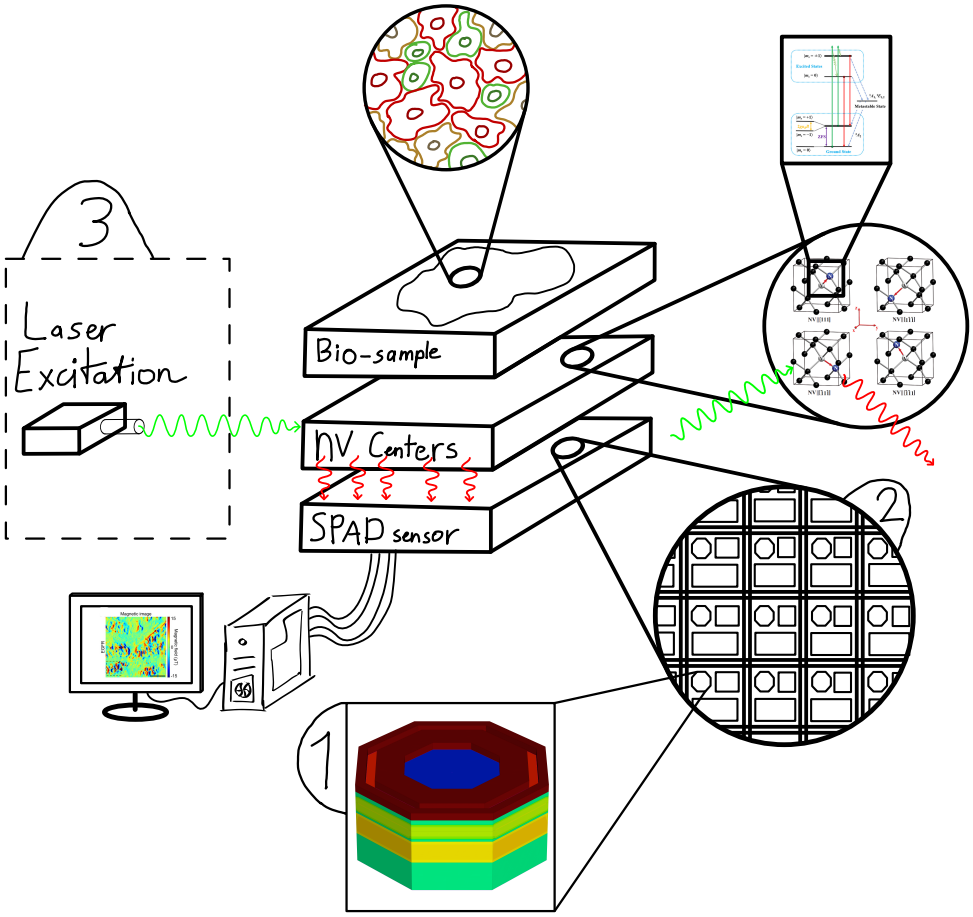

Figure 1.1: General overview of the full system used for magnetic bioimaging, showing the main components of the systems, the bio-sample, NV centers, laser excitation system, and SPAD sensor.

1.2. THEORY

The theoretical background required for understanding the remainder of the report is discussed in the following section. Firstly, the SPAD and its working principles are explained. Next, the concept of quenching and a simple quenching circuit will be described in detail. Finally, the basic principles and properties of NV centers in diamond will be introduced.

1.2.1. SPAD

A SPAD is a photodiode that is connected by placing a positive voltage on the cathode, placing it in a reverse bias. Furthermore, the applied bias voltage is above the first breakdown voltage, but usually below the second breakdown, placing it in the Geiger-mode region [14]. Fig. 1.2 illustrates the region on an I-V curve where the diode operates in

Geiger-mode. In this mode, a negligible quiescent current flows through the SPAD. However, a single incident photon that reaches the depletion region can initiate an avalanche current. The driving force of the avalanche current is impact ionisation. Under a large enough electric field, a free charge carrier generated by an incident photon is quickly accelerated. When the free charge carrier has enough kinetic energy it can create more free charge carriers on impact with other atoms, producing a rapidly increasing current that can be detected. This process allows the SPAD to detect the arrival of a single photon with a resolution of picoseconds. The avalanche current, which can reach several milliamperes, needs to be stopped through a process called quenching. This is to make sure that the SPAD remains undamaged and the next photon can be detected. The avalanche current is interrupted by an aptly named quenching circuit, which lowers the voltage drop across the SPAD so that it is biased below or equal to the breakdown voltage, lowering the strength of the electric field in the depletion region. The SPAD is subsequently recharged and ready to detect the next photon. This process is shown in Fig. 1.4. [15].

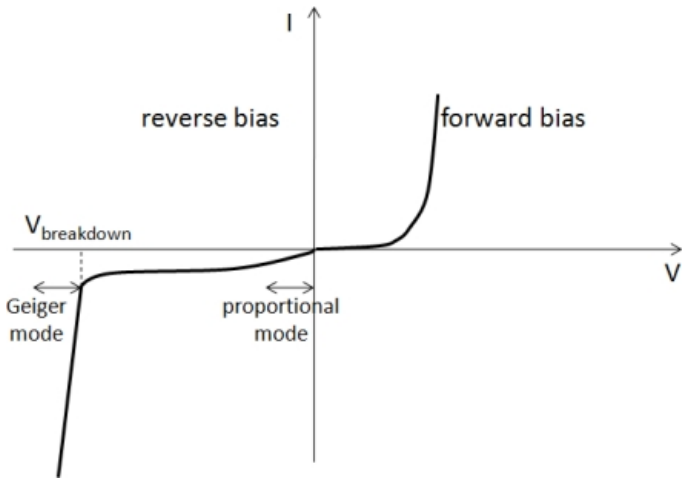

Figure 1.2: I-V curve with the positive voltage applied to the anode showing Geiger mode operation. Taken from Spanoudaki et al. [16]

For the SPAD to function, it must be biased above the breakdown voltage V_B. A bias supply voltage V_A is used for this, providing an excess voltage V_E above breakdown. Thus $V_E = V_A - V_B$ since the excess voltage is equal to the difference between the supply voltage and the breakdown voltage. The performance of the SPAD is directly influenced by the excess voltage with respect to the breakdown voltage since it establishes the excess electric field [17].

1.2.2. QUENCHING

SPADs require quenching circuits to terminate the avalanche current to prevent harm to the diode and for it to be able to detect the next photon. There are two methods of quenching: passive and active quenching, each having performance and complexity trade-offs. Active quenching utilizes transistors and feedback loops for the quenching,

which allows for fast photon detection and an adjustable dead time. However active quenching requires complex circuitry making it harder to implement, as it requires more area and power [18].
Passive quenching uses a high impedance (50k-1MΩ) resistor in series with the SPAD to quench off the avalanche current. Simplicity is a big advantage of passive quenching as only passive elements, such as resistors, are used, which also leads to a lower area occupation. The downside of using passive quenching is the non-controllable hold-off time, meaning you cannot control when the next photon can be detected by the SPAD [15].

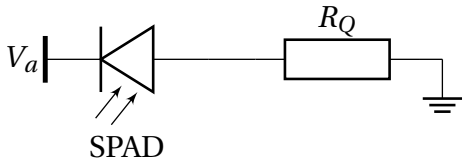

Figure 1.3: Passive quenching circuit with a SPAD and a quenching resistor

The simplest passive quenching circuit is a SPAD in series with a resistor. A simple quenching circuit can be seen in Fig. 1.3. When a photon is detected and an avalanche current spikes, there will be a voltage drop over the quenching resistor. This voltage drop then lowers the voltage across the SPAD, biasing it below its breakdown voltage and turning it 'off' again by quenching the avalanche current. This process is seen in Fig. 1.4.

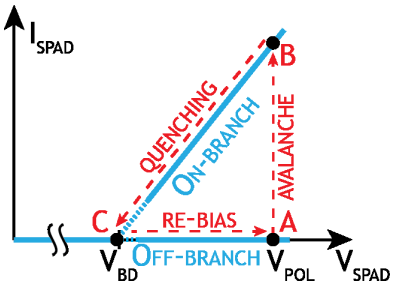

Figure 1.4: Current vs Voltage (I-V) characteristics of the SPAD during operation. V_{BD} is the breakdown voltage. The voltage is raised past the breakdown voltage until a photon is detected, point A, triggering an avalanche. The current rises up to point B after which the quenching will start lowering the voltage to below the breakdown voltage, point C. Taken from Bronzi et al. [19]

The quenching resistor R_Q must be large enough to quench off the avalanche current. If I_R is the current through the quenching resistor then this must be lower then the latch current, which is the current at which the avalanche is self-sustaining. Thus, $I_R = \frac{V_E}{R_Q}$ must be smaller then this latch current. The value of the latch current is not exactly defined due to jitter in the quenching time. However, an estimation of a current equal to or smaller then 100 μA was made [17]. When the current remains below this

level the avalanche current through the SPAD is consistently quenched off.
After quenching, the diode voltage recovers towards the bias voltage with a characteristic time constant T_r, which is determined by the product of the quenching resistor R_Q and the total capacitance of the SPAD. The total capacitance consists of the junction capacitance C_D and any stray capacitance C_S. So $T_r = R_Q(C_d + C_s)$ and is usually in the range of micro seconds during which the voltage across the diode gradually rises above the breakdown voltage [17]. During the first part of the recovery, the probability of detecting incoming photons is very low, and most photons are effectively lost. As the voltage over the diode increases, the likelihood of triggering an avalanche due to an incoming photon increases as well. Since new photons can only be successfully detected once the diode voltage has sufficiently recovered, the recovery time has a significant impact on the overall photon counting efficiency [17].

1.2.3. NV CENTERS

In our application SPADs are used to detect single photons emitted by NV centers in diamonds. NV centers are point defects found in diamond. These consist of a vacancy in the diamond crystal lattice adjacent to a nitrogen atom. Another term for this is an NV^0 center. The nitrogen atom can capture an additional electron to form a negatively charged NV^- center. NV^- centers are particularly useful in our application, because of their comparatively long coherence time, ability to function at a wide range of temperatures, and the ability to be optically initialized and read-out. For simplicity we will refer to the NV^- center as just the NV center from now on [20].

When excited with a green laser with a wavelength of 532 nm, the electrons move from the ground state to the excited state. This process is spin-conserving so when an electron is in $|0, g\rangle$ it will move to $|0, e\rangle$ and like wise for $|\pm1, g\rangle$ moving to $|\pm1, e\rangle$. To go back to the ground state the electron can emit a red photon, with a wavelength of 600 to 850 nm. When an electron is in the $|\pm1, e\rangle$ state it can also decay non-radiative through the shelving state. During this process infra-red light will be emitted. This process is not spin-conserving as the electron predominantly ends up in the $|0, g\rangle$ state. This phenomenon makes it that the spin-states of the NV centers can be initialized. Electrons from the $|0, g\rangle$ state will cycle between $|0, g\rangle$ and $|0, e\rangle$ during a radiative cycle. On the other hand electrons in the $|\pm1, g\rangle$ state can excite to $|\pm1, e\rangle$ after and back to $|\pm1, g\rangle$, but can also end up in $|s\rangle$ from $|\pm1, e\rangle$ after which it decays back to $|0, g\rangle$. By exciting a green laser on the NV center for long enough, typically in the microsecond range, about 95% of all electrons will end up in the $|0, g\rangle$ state [21]. After initializing the system like this it makes it that it can be read-out optically [22], [23].

ENERGY LEVEL DIAGRAM

The NV center contains two unpaired electrons originating from the nitrogen atom and the vacancy. Four different configurations of spin states can be created by these two electrons: three triplet states and one singlet state. The ground state and excited state make up the triplet configurations, $m_s = 0, \pm1$, whilst the shelving state is the singlet state [24]. Fig. 1.5 shows the energy level diagram of the NV center. It consists of a ground state, excited state and a shelving state. All these energy levels fall within the energy band gap of the diamond. Without the presence of an external magnetic field there are three spin

states $m_s = 0$ and $m_s = \pm 1$, where the latter states are degenerate. When an external magnetic field is present, zero field splitting occurs, splitting the $m_s = \pm 1$ spin subsystems into separate energy levels [21].

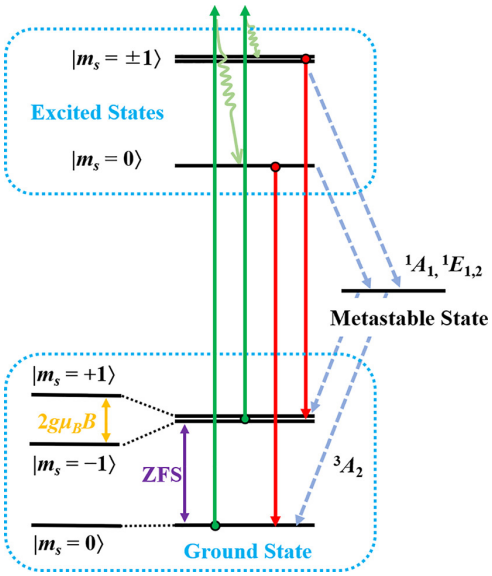

Figure 1.5: Energy level diagram of the NV center with B>0, resulting in zero field splitting. Taken from Song et al. [25]

CW ODMR AND ZEEMAN EFFECT

Now that the basic principles of NV centers have been explained we can go on to how we measure these NV centers. When an electron decays through the shelving state, there will be less fluorescence as this path is nonradiative. By measuring the fluorescence the spin state can be determined, as there will be less fluorescence when the electron is in $|\pm 1\rangle$. By applying a continuous wave (CW) an optically-detected magnetic resonance (ODMR) spectrum can be created. When the microwave frequency is equal to the resonance frequency we observe a dip in the ODMR spectrum, which is a reduction in the fluorescence. This is because the electron population transfers from $|0, g\rangle$, bright state, to $|\pm 1, g\rangle$, dark state. At room temperature this occurs at 2.87 GHz. When using CW ODMR the maximum amount of the population transferred to the dark state depends on the power of the microwave and laser, but the maximum is 30% of the count rate corresponding to the fluorescence of the bright state [21]. By applying an external magnetic field, B_0, the energy levels $|\pm 1\rangle$ are split, as they can be oriented parallel or anti-parallel to the magnetic field vector. The electron spin's quantum-mechanical properties are what cause the energy levels to become quantized. The spin Hamilton operator describes the potential energy of this system and is derived from the classical expression for the energy

of a magnetic dipole in a magnetic field and its expressed in Hertz:

$$H = g_e \frac{\beta_e}{h} \boldsymbol{B_0 S} \tag{1.1}$$

g_e is the g-value of the free electron, β_e is the Bohr Magneton, h is plancks constant, $\boldsymbol{B_0}$ is the applied external magnetic field and $\boldsymbol{S}$ is the spin [26]. Due to the Zeeman effect, which causes the energy levels to split by applying an external magnetic field, there is not one but two dips in the ODMR spectrum from the -1 and +1 states respectively. By measuring the distance between these two dips the magnetic field along the direction of the quantization axis can be determined. Equation 1.2 shows this relation.

$$B = \frac{h}{2g_e\mu_h}\Delta\nu \tag{1.2}$$

The frequency splitting $\Delta\nu$ and the magnetic field B are only dependent on constants which are the same for all NV centers, so when measuring the sensor does not have to be recalibrated when measuring a different NV center [21].

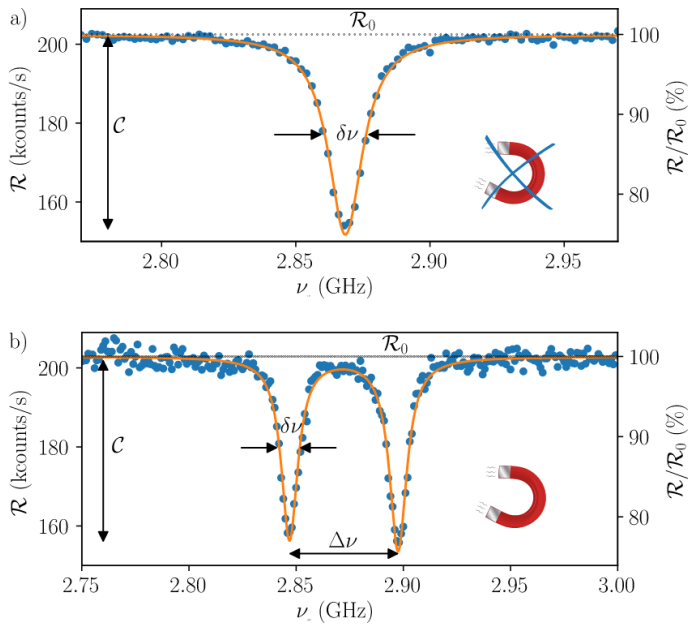

Figure 1.6: Fluorescence spectra of NV centers a) without an external field present with only a single dip at 2.87 GHz and b) with an external field present causing Zeeman splitting which can be seen by the two resonance dips in the graph. Taken from *Qnami* [21]

1.3. THESIS SYNOPSIS

This thesis starts by providing the programme of requirements necessary for characterizing the SPAD in chapter 2. In chapter 3 a 3D model of the SPAD is designed and simulated

to obtain the I-V and C-V curves. The physical SPAD is validated in chapter 4 and a new ADC for the SPAD readout is designed in chapter 5. Finally in chapter 6 a conclusion is made in which recommendations are given for future work.

2

PROGRAMME OF REQUIREMENTS

The goal of this project is to firstly, create a model of the SPAD in TCAD such that the Current vs Voltage (I-V) and Capacitance vs Voltage (C-V) curves can be simulated. Next, the physical SPAD that is present in the current fabricated IC will be validated to determine if this design works as a valid SPAD or not. A testing set-up will be designed to accomplish this. Finally, a new improved Analog to Digital Converter (ADC) will be designed and tested which can be implemented on the IC by the Integration and Optimization group.

2.1. SPAD MODEL AND SIMULATION

A viable model and corresponding simulations are important to determine if a design works as intended. For this, the following is required:

- A 3D model of the SPAD
- I-V and C-V simulations along an applied cathode voltage of up to 40V

This should provide ample information to be able to verify if the design is valid or not.

2.2. PHYSICAL SPAD VALIDATION

For the physical SPAD validation the stray SPADs on the chip will be used, as they can be tested by themselves. A new testing circuit will be created on the PCB the SPAD chip is mounted on. To confirm whether the SPADs work the breakdown voltages will be tested first. If this works the photon detection is tested. When current pulses are seen we can confirm that the SPAD can detect photons and they work as expected, so the problem of them not working lies elsewhere. Below are the values that should be found during testing. When the values deviate from these by a lot we can assume that the SPADs do work but just not as they should. The values of the breakdown voltage were measured during Dylan's master thesis [12].

- Reverse breakdown of approximately 16V
- Forward voltage of approximately 3V
- Current pulses of 10 to 100 ns

2.3. ADC

A new ADC using a Schmitt trigger is designed for better performance at high frequencies. The new ADC has several requirements it has to meet:

- Have low enough propagation delay, max 25 ns, to detect fast current spikes in the range of 20 to 100 ns
- Have voltage thresholds in the range of 0.5 to 2V

This should provide sufficient data to verify if Schmitt triggers are the better choice for the ADC used in combination with the SPAD.

3

SPAD MODEL AND SIMULATION

Modeling and simulating a SPAD is circuit simulation at the component level, with the focus on the behavior of the SPAD itself. To achieve this, the SPAD will be simulated using several tools included the Synopsis TCAD Sentaurus suite [27], which allows for simulation of the semiconductor device itself. TCAD, or Technology Computer Aided Design, is software which allows for the simulation of manufacturing processes and device simulations to determine physical parameters and electrical behavior.

In this chapter we will discuss the creation of a viable SPAD model given the previous design by Van Rijs et al. [28] and the Integration and Optimization group with several assumptions that were made about the manufacturing process. Next the process for the creation of the SPAD models in Sentaurus Structure Editor (sde) and the setup for the I-V and C-V device simulations in Sentaurus Device (sdevice) are given. Finally, the results of the structure creation and device simulation are shown.

3.1. SPAD DESIGNS

To simulate the SPAD as a semiconductor device, a model of the device is required. This model has to be as close to the finished product as possible to obtain accurate simulation results. To achieve this, a 3D model of a SPAD design will be created. Previously, the QIT group has designed several different SPAD layouts based upon a cross-section by Perenzoni et al. [29, Fig. 1a]. Yet after further inspection of the layout of the IC designed by Van Rijs et al. [28] in Cadence Virtuoso, the industry standard IC design software, it has been found that the final implemented cross-section of the SPADs resembled the structure seen in Fig. 3.1a, which differs slightly from the design by Perenzoni et al. [29]. There is an N-well missing underneath the P+ contact point, the N+ contact points are wider than the outer N-well, and the width of the Deep N-well (DNW) is less than the outer edges of the outer N-well. These differences can, and will, affect the performance and behaviour of the SPAD. Additionally, it is to be noted that the P region in between the P+ contact and the DNW is not an explicit P-type doping region, but the P substrate.

Furthermore, there are two different symmetries for the SPADs that were designed, a rectangular one and an approximately circular one. The latter one of these consists of multiple rectangles stacked on top of one another in the layout, making it such that it appears as a round layout. The performance of the approximately circular layout is expected not to differ a lot from the rectangular one, as such only the SPAD with rectangular symmetry will be modeled.

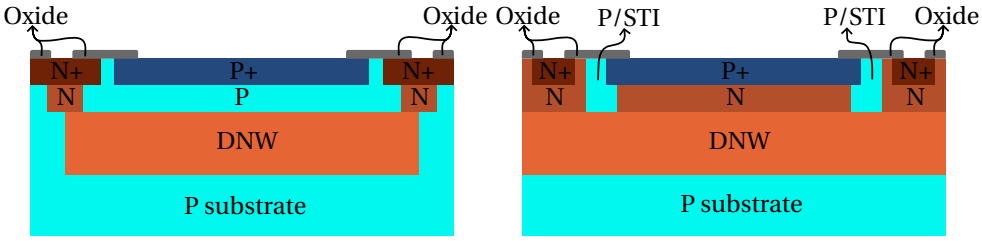

(a) Cross-section of the SPAD designed by Van Rijs et al. [28] which is present on the current IC

(b) Cross-section of the SPAD designed by the Integration and Optimization group

Figure 3.1: The different designed SPAD cross-sections on which the 3D model is based

Alternatively, the cross-section of the design proposed by the Integration and Optimization group is seen in Fig. 3.1b. This design is also correctly reflected in the layout created in Cadence Virtuoso and as such adheres more closely to that of Perenzoni et al. [29]. Additionally, the layout shows the SPAD having octagonal symmetry, providing a common ground between a fully circular design and a rectangular design. Furthermore, according to the TSMC design rules [30], a Shallow Trench Isolation (STI) section made of silicon-oxide is also implemented. This differs from the design laid out by Perenzoni et al. [29]. For consistency, both the model with STI and without will be considered.

3.1.1. ASSUMPTIONS MADE FOR THE SPAD MODEL

Given that we do not have exact information about the TSMC 40nm fabrication process, some assumptions have to be made in order to make a 3D SPAD device model. Two different doping profiles will be evaluated: an ideal constant doping profile and analytic doping profiles. For the latter option it was assumed that the regions were created using ion implantation and follow a gaussian retrograde profile characteristic to ion implantation [31]. Furthermore, the following target doping concentrations were used: a P substrate and N-well doping concentration in the order of 10^{15}cm^{-3}, a DNW doping concentration in the order of 10^{19}cm^{-3}, and a P+ and N+ doping concentration in the order of 10^{21}cm^{-3}. These are the same for both the constant doping profiles and the analytic profiles, with an exception for the N-well for the analytic doping profiles, where the peak concentration was made to be $1\cdot10^{16}\text{cm}^{-3}$ to account for the retrograde profile. More detail on the assumptions made can be found in section C.1.

3.1.2. METHODS

To create the models for the SPAD designs, the Sentarus Structure Editor (sde) tool was used. To create the model, the Sentauruse Structure Editor user guide was followed [32]. Half of the cross-sections described in Fig. 3.1 was made and subsequently revolved around either a square path or an octagonal path, creating the full 3D structures. Afterwards, the contacts and doping profiles were assigned accordingly, following the target concentrations laid out before. The full list of used command files used for the sde tool can be found in section B.1.

For device simulation, the program Sentaurus Device (sdevice) was used. Following examples presented with the software and the Sentaurus Device user guide [33], the sim-

ulations were set up. For determining the I-V curves, the Van Overstraeten Avalanche generation model [34] was used in combination with Shockley-Read-Hall recombination [35] based upon the doping concentration. The carrier generation model calculates the amount of generated charge carriers, and thus current, based upon the electric field strength. However, at very high values of the electric field the model becomes unreliable, yet in our case those values are beyond what needs to be measured. On the other hand, Shockley-Read-Hall recombination is one of the main recombination models and valid in all cases due to point defects in the semiconductor.
During the I-V simulations, the initial device conditions are calculated first. Next the cathode voltage is ramped up to a desired goal to determine the I-V curve, calculating device conditions at each timestep.
To obtain C-V curves, an AC small-signal analysis between frequencies of 10kHz and 1MHz performed, obtaining the averaged capacitance and admittance matrices. The used command files for the sdevice tool can be found in section B.2.

To visualise the device structures and the simulated I-V and C-V curves were visualised using Sentaurus Visual (svisual). The creation of the graphs and images using svisual was done by hand for each required graph or image, given the low volume of steps and visualisations required.

3.2. 3D SPAD MODEL AND DOPING PROFILES

After creation of the 3D SPAD models, their structure was visualised using svisual. Given the fact that the 3D models have regions that are enclosed within the structure, both a 3D render as well as a cross-section are shown. Additionally, the doping profiles of the structures are shown using a heatmap, where the negative doping profiles are indicated with a more red colour and the positive doping profiles are indicated with a more blue colour. Any oxide regions however are indicated by a constant dark red colour. Finally, only the structures with analytic functions assigned for their doping profiles are shown, as the structures with constant doping profiles only differ in their doping profiles.

The 3D model of the rectangular SPAD with analytic doping profiles can be seen in Fig. 3.2a. This also shows the plane along which the cross-section seen in Fig. 3.2b is made. As can be seen, there are several clearly defined dopant regions, even with the analytic doping profiles and the possibility of diffusion of dopant atoms into beyond their designated regions. Additionally, there are some rectangles that can be seen in the cross-section. These are indicative of the designed doping locations that can also be seen in Fig. 3.1a.

The 3D model of the octagonal SPAD can be seen in Fig. 3.3a. As can be seen, there is a some significant differences when compared to the previous design. One of the main parts is the octagonal instead of rectangular symmetry. Furthermore, the doping locations of the cross-section seen in Fig. 3.3b adhere to the design shown in Fig. 3.1b, with the constant doping profiles following the same methods and results as with the SPAD with rectangular symmetry above. Lastly, a second cross-section is shown in Fig. 3.3c with STI regions.

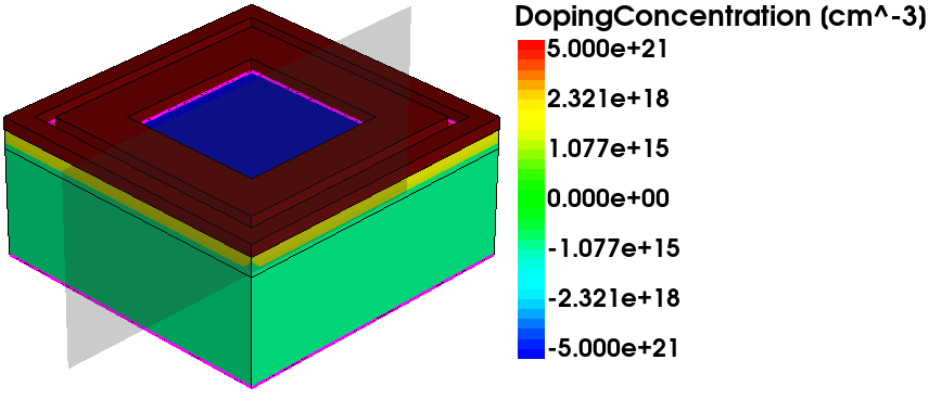

(a) 3D image of the rectangular SPAD model

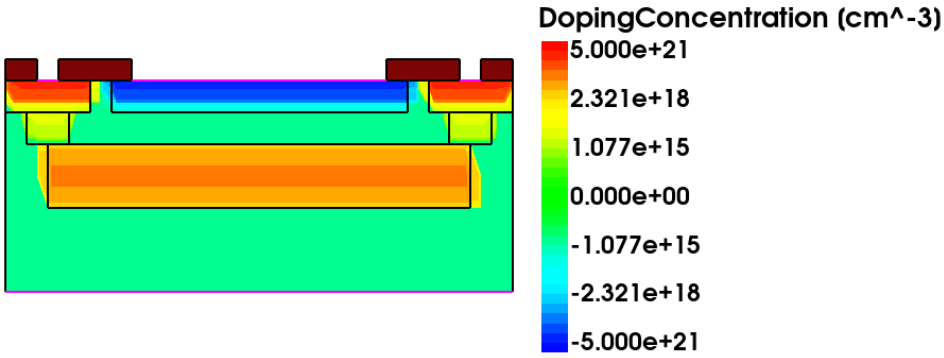

(b) 2D cross-section of the rectangular SPAD

Figure 3.2: 3D model of the rectangular SPAD with analytic doping profiles

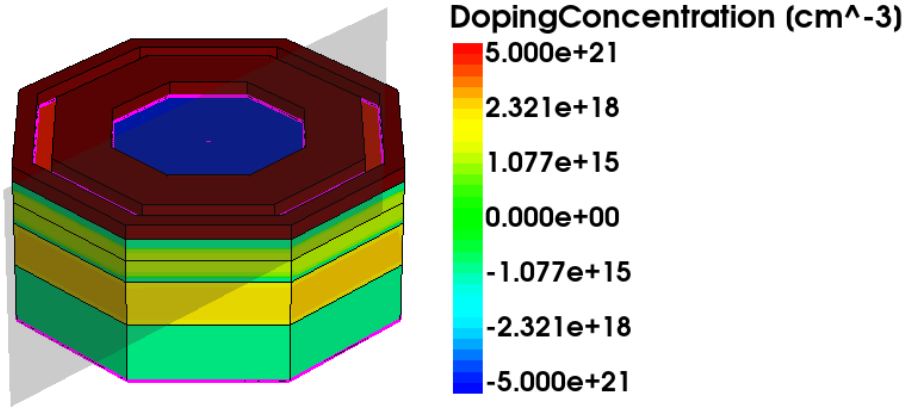

(a) 3D image of the octagonal SPAD model

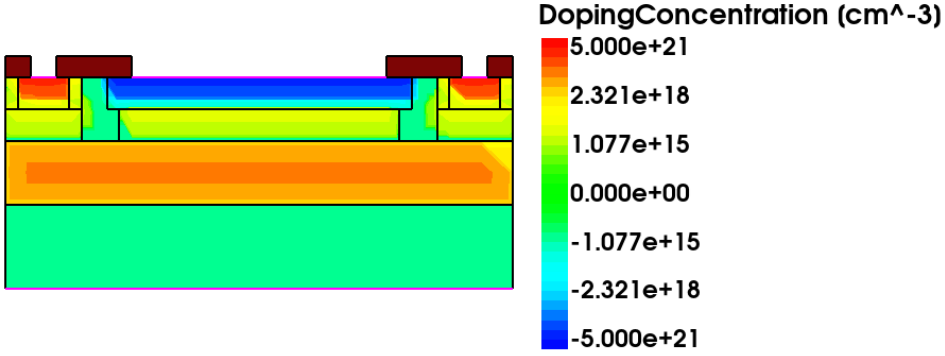

(b) 2D cross-section of the octagonal SPAD without STI regions defined

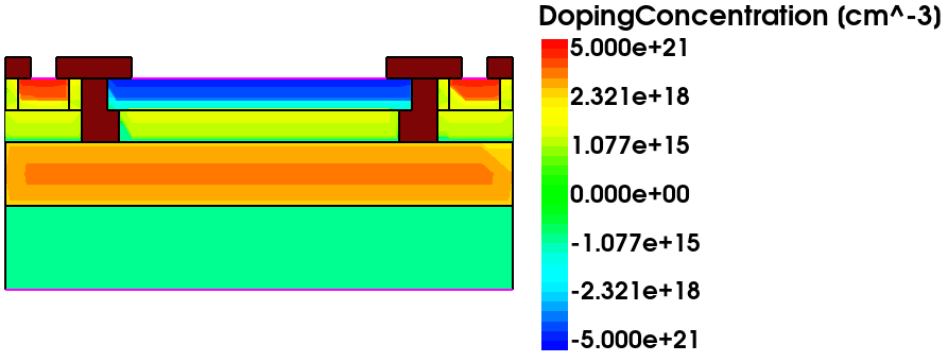

(c) 2D cross-section of the octagonal SPAD with STI regions defined

Figure 3.3: 3D model of the octagonal SPAD with analytic doping profiles

3.3. I-V CURVES

After the I-V simulations were finished, their results were graphed using svisual. For each of the simulations a separate graph was made. Except for the octagonal SPAD with analytic doping profiles, as this has two options with just a slight difference, including an STI region and not. As such, these two options are shown together.

The I-V simulation results for the SPAD with rectangular symmetry are shown in Fig. 3.4. In Fig. 3.4a the I-V simulation results can be seen for the rectangular SPAD with constant doping profiles. As can be seen, the cathode current remains relatively smooth and becomes very irregular at higher voltages. Additionally, the extents of the y-axis has been limited as the irregularities are not as important. As can be seen there is a clear increase in reverse bias current that can be seen at an applied cathode voltage of approximately V_C =7.5V. For the I-V simulation results for the rectangular SPAD with analytic doping profiles seen in Fig. 3.4b a more smooth curve can be seen, with irregularities forming above V_C =22V. Here an increase of the reverse bias current can be seen at approximately V_C =9V.

In Fig. 3.5 the simulation results can be seen for the SPAD with octagonal symmetry. The results for the octagonal SPAD with constant doping profiles can be seen in Fig. 3.5a. It can be seen that approximately at V_C =6V the reverse bias current has a large increase and afterwards it levels out.

The results of the I-V simulation of the octagonal SPAD with analytic doping profiles can be seen in Fig. 3.5b. Both the devices including and excluding an STI region are seen in the same graph. As can be seen, both options show a similar increase in reverse bias current at approximately V_C =7V. Additionally, the device with an STI region, shown as the green trace, shows a second increase in current at approximately V_C =14V, which keeps increasing from that point onwards. The graph however has been limited in order to show the difference between the device with and without an STI region. The full graph can be seen in Fig. A.1. Without the STI region however, shown as the red trace, the device shows an irregular current above V_C =20V and no second sudden increase in reverse bias current

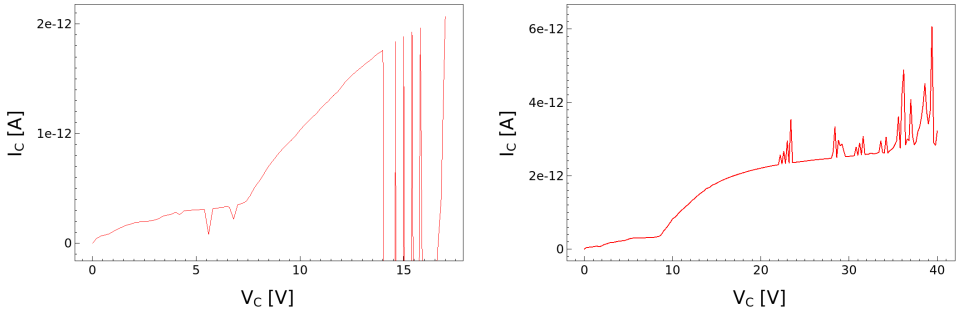

(a) Rectangular SPAD with constant doping profiles

(b) Rectangular SPAD with analytic doping profiles

Figure 3.4: I-V curves for the rectangular SPAD models

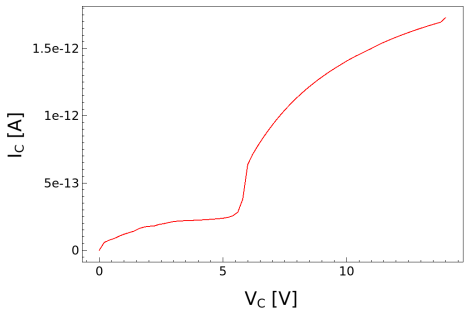

(a) Octagonal SPAD with constant doping profiles

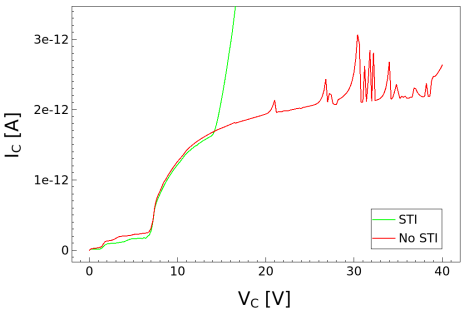

(b) Octangonal SPAD with analytic doping profiles

Figure 3.5: I-V curves for the octagonal SPAD models

3.4. C-V CURVES

After the C-V simulations were finished, their results were graphed using svisual. For each of the simulations a separate graph was made, showing three different capacitances are shown, the anode-cathode capacitance C_{AC}, the cathode-substrate capacitance C_{CS}, and the anode-substrate capacitance C_{AS}.

The graphs with the C-V curves for both the rectangular and octagonal SPAD models with analytic are shown in Fig. 3.6. It can be seen that both the C-V curves show a negative capacitance value for each of the capacitances. This is not expected, as a positive capacitance value is expected from the SPADs. Furthermore, the rest of the C-V simulations showed approximately the same curves, and possibly with more erratic and unexpected behaviour. These can be seen in Fig. A.2-A.4.

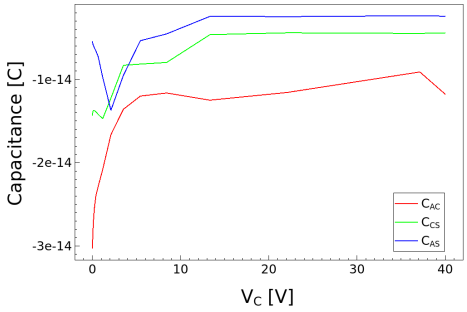

(a) C-V curve of the rectangular SPAD

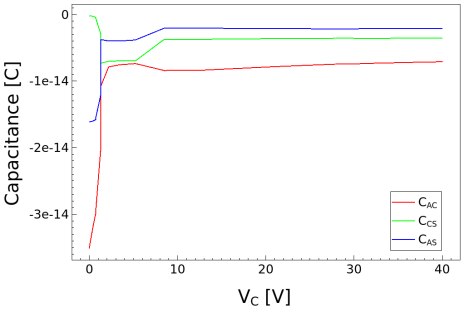

(b) C-V curve of the octagonal SPAD without STI regions

Figure 3.6: C-V curves for the rectangular and octagonal SPAD models with analytic doping profiles

3.5. DISCUSSION

From the graphs in Fig. 3.4a and Fig. 3.5a it is difficult to concisely determine the breakdown voltage V_{BR}. However, using these simulations it is possible to see the approximate behaviour that is to be expected from the devices. Additionally, the simulation for

the octagonal SPAD with analytic doping profiles and STI included clearly shows predictable reverse behaviour. Yet, when comparing the two traces seen in Fig. 3.5b it can be seen that when no STI region is included, erratic behaviour occurs at higher applied bias voltages. This can be attributed to a limitation of the Van Overstraeten model, which becomes invalid when a stronger electric field is applied. However, for the purpose of determining the breakdown voltage and the general I-V characteristic, the model remains valid. Additionally, a SPAD has a dark count rate, where spontaneous carrier generation induces an avalanche current. This dark count rate increases with higher bias voltages applied. It is a possibility that the erratic behaviour can be attributed to this behaviour. However, this is very unlikely as only the avalanche carrier generation model is called.

The C-V curves that have been generated after simulation show a negative capacitance, which was unexpected. However, negative capacitances are a phenomena that can occur in devices that employ strong electric fields at high enough frequencies [36]. Given the comparably small nature of the previously manufactured and currently proposed SPAD design compared to the p-i-n diode seen in [36], it is possible that for our capacitance measurements between the frequencies of 10kHz and 1MHz already result in a negative capacitance in the device. Nonetheless, the measurements made show relatively erratic and unconsistent behaviour throughout the simulated voltage range.

4

SPAD VALIDATION

In this chapter the stray SPADs which are mounted onto the PCB are validated. In previous work [12], [13], [28] the SPADs didn't work as intended. So in this chapter we will try to figure out what could have gone wrong by creating a new testing circuit for the stray SPADs and validate them through two steps: first find the correct breakdown voltages and secondly test the quenching. In the end a conclusion can be made whether the SPADs themselves do not work or that the problem is in the surrounding circuitry.

4.1. CURRENT DESIGN

The SPADs utilized during this project were designed two years ago by a previous BAP group together with researches from QIT [28]. Since then this design has been used in the production of all physical SPADs being used during our project. The devices were designed using Cadence, however, it's important to note that no verification or simulations of this SPAD chip were done to our knowledge prior to fabrication.
Our first step involved a detailed analysis of a single SPAD and how these were connected in the testing circuit. A significant design flaw was discovered during this analysis: the SPADs were configured to operate in forward bias instead of reverse bias, which is the correct operational mode for avalanche photodiodes. The diode has a radial PN-junction meaning the inner area is P-type and the ring around is N-type.
Using the theory obtained in semiconductor physics we know that in an PN-junction the current flows from the P-type to the N-type when in forward bias. The applied bias voltage (V_a) is connected to the inner P-type area, confirming that the device is indeed forward biased [37]. Fig. 4.1 shows a schematic representation of the SPAD operation, in forward bias, of the current design.

4.2. MEASUREMENT SET-UP

To confirm our suspicion that the SPADs were forwards biased a test circuit was developed. Given that the SPADs are permanently mounted onto the PCB, which can be seen in Fig. A.5, some modifications were implemented directly on this board:

- All components were desoldered
- A quenching resistor, R_Q, was added between V_a and ground
- The bias voltage application point was moved to V_{out}, which previously was the output node

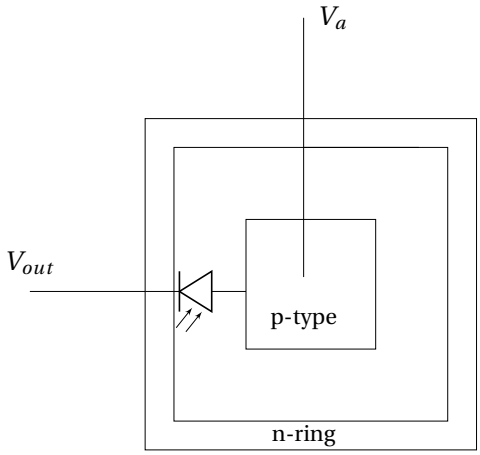

Figure 4.1: Schematic representation of the SPAD operation in forward bias. The voltage is applied to the middle of the SPAD meaning the current flows from inside, P-type, to the outside, N-type, of the SPAD [37].

The revised topology, shown in Fig. 4.2, allows for testing the stray SPAD in reverse bias. An oscilloscope is placed over the quenching resistor to measure the voltage over it.
The tests are done in two phases: the first to confirm that the stray SPADs are now indeed reversed biased and the second to see if photons are detected. During the first test the applied bias voltage is gradually increased until the reverse breakdown voltage is reached and current will be conducted. This will be seen by a voltage drop over the quenching resistor measured by the oscilloscope. In the second test the quenching is tested. This test will be conducted in the dark, so that only the Dark Count Rate, DCR, is present. An avalanche can be triggered within the SPAD due to non-photon generated carriers which is characterized by the DCR. For our SPAD the DCR should be in the range of 200 counts per second [38], [39]. During these tests an oscilloscope is used with a frequency of 12.5 MHz so that a single avalanche with quench can be seen, this equal to 80 ns which is fast enough to detect the avalanche and quenching.

4.3. RESULTS

The first experiment confirmed the SPADs' operational bias characteristics through testing with the new circuit. The following values for the breakdown voltage were found:

- **Reverse breakdown voltage**: 16.8V, typical for SPADs [17]
- **Forward voltage**: 0.9V

When reversed biased above the breakdown voltage a voltage drop equal to the excess voltage, applied bias voltage minus breakdown voltage, was seen over the quenching resistor. This test was conducted illuminated with an oscilloscope not fast enough to detect the avalanche and quenching which might explain the self-sustaining avalanche current that we saw.
The second test conducted used a faster oscilloscope which could detect the voltage

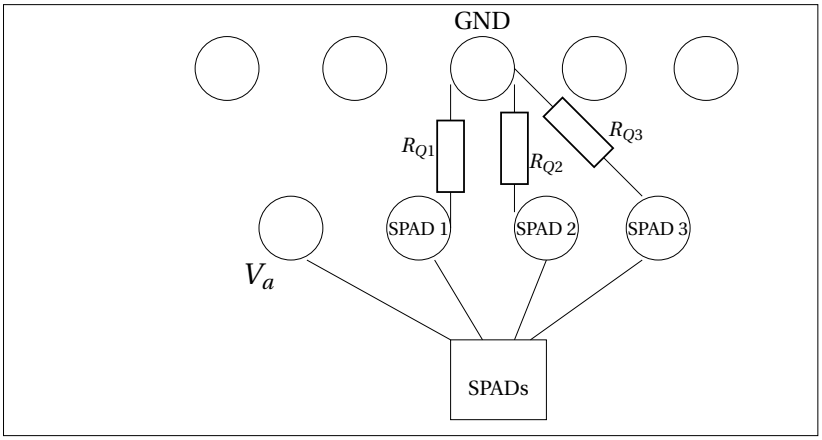

Figure 4.2: Test circuit used to validate stray SPADS. R_Q's are quenching resistors. The PCB previously used can be seen in Fig. A.5

pulses created by the avalanche current in the nano second range. As explained in the previous section this test was conducted in the dark so that only the DCR would cause avalanches, which is better to measure then when illuminated. The device demonstrated continuous conduction when biased above breakdown voltage, zero DCR, and a static voltage drop approximately equal to the excess voltage. From these results we can conclude that the SPADs don't work. The results can be seen in Fig. 4.3. In this figure it is clearly visible that when biased above breakdown voltage a static voltage drop, approximately equal to the excess voltage, is seen over the quenching resistor.

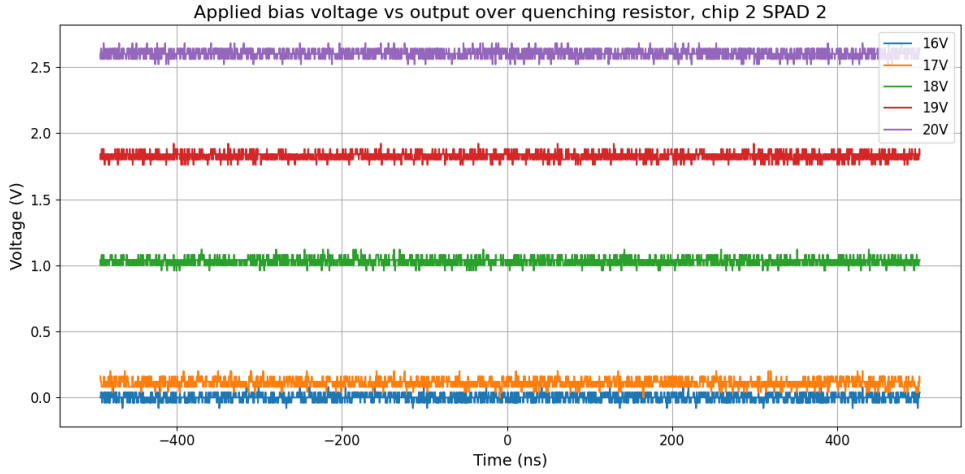

Figure 4.3: Applied bias voltage versus the output it gives over the quenching resistor. Chip 2 stray SPAD 2 was used for this measurement with a breakdown voltage equal to 16.8V

4.4. DESIGN FLAW

A design error was identified in the original SPAD structure: the absence of an N-well between the P+ region and the DNW. This missing N-well significantly weakens the electric field within the device. As a result, the depletion region is not fully depleted of charge carriers, the SPAD is unable to detect photons properly and conducts continuously when biased over the breakdown voltage. This problem has been resolved in the updated design, which was created by the Integration and Optimization group, by adding the required N-well. Fig. 3.1 shows on the left the cross section without the N-well and on the right the cross section of the SPAD designed by the Integration and Optimization group. During simulation a relatively low breakdown voltage was found, of 7V, which is a lot lower then the expected breakdown voltage that is at least 10V. Fig. 4.4 highlights the location missing N-well and shows the resulting lower breakdown voltage.

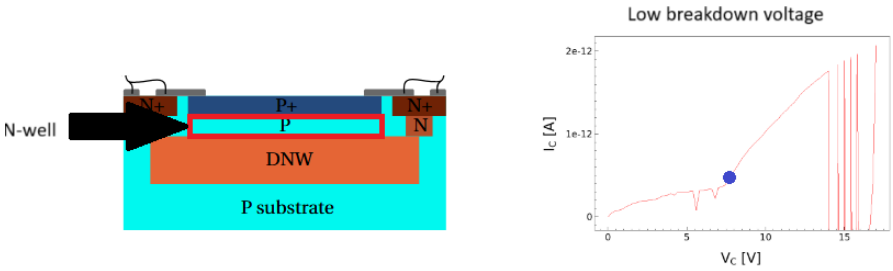

Figure 4.4: On the left the SPAD cross section from 2023 design with the area where the missing N-well should be highlighted with a red box [28] and the resulting lower breakdown voltage highlighted with a blue dot on the right.

5

Analog to Digital Converter

An ADC, analog-to-digital converter, is needed to convert the current spikes of the detected photons into digital output pulses that can be used in further processing. In previous projects a comparator was used for this. This comparator was designed in 2023 [13] and has not been changed since. In their report they discussed the possibility of using a Schmitt trigger instead of a comparator, but opted for the latter as this was the simpler design. We believe a Schmitt trigger has a far better chance of succeeding then the comparator when combined with the SPAD. In this section we will discuss why a Schmitt trigger is the better option, the circuit designed, the simulations of said circuit and the test results.

5.1. Comparator vs Schmitt trigger

A comparator is a device which compares an input voltages to a set threshold voltage, giving a digital output pulse whenever the input voltage exceeds the threshold voltage. A digital output pulse is needed as this can directly be fed to digital signal processing circuitry or digital devices such as FPGA's unlike operational amplifiers that have an analog output [40]. In the previous design they opted for a comparator because of its simplicity and easily tuneable threshold voltage [13]. The previous design can be seen in Fig. A.6
However, a notable drawback of using a comparator in combination with a SPAD is their inability of handling noisy input signals. Comparators only posses a built-in hysteresis level of about 10 mV, making them subject to false output triggers due to small fluctuations in the input signal caused by noise. A Schmitt trigger has been suggested as a solution to this problem. While comparators and Schmitt triggers share similar circuits, the addition of positive feedback to a comparator adds hysteresis, in doing so creating a Schmitt trigger.
Hysteresis is essentially a buffer that prevents small deviations in the input signal, such as noise, from changing its output pulse. Schmitt triggers are especially suited for processing the short, noisy pulses generated by SPADs. Two separate threshold values are generated by the positive feedback: a lower threshold for switching the output low and a larger threshold for switching the output high. As a result the output only changes states when the input signal crosses its respective threshold, thereby improving noise immunity [41]. Fig. 5.1 shows the difference between comparators and Schmitt triggers, due to the added hysteresis. Another advantage of the Schmitt trigger is its sharp edges in the output pulses, making it a clean output signal which is ideal for photon counting [42].

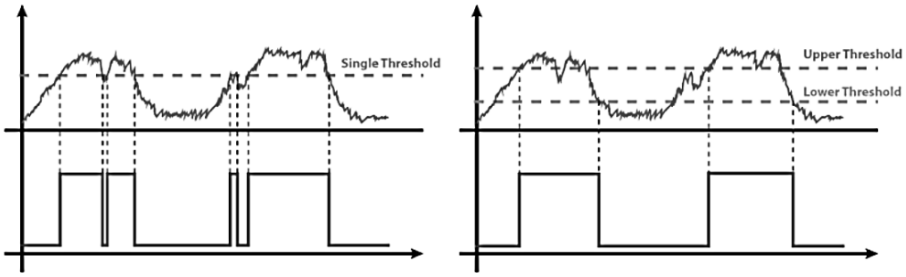

Figure 5.1: Comparator output on the left without hysteresis. Schmitt trigger output on the right with hysteresis. This can be seen by the output not immediately switching after noise causes the input signal to below the upper threshold value. Taken from *Cadence PCB Solutions* [41]

5.2. ADC CIRCUIT

The first design choice involved selecting an appropriate Schmitt trigger for our circuit. In 2023 a Schmitt trigger wasn't used, as they thought the signal from the SPAD would need biasing and amplification [13]. In our approach we avoid the need for biasing and amplification. The Schmitt trigger needs to meet several requirements:

- **Propagation delay**: The delay must be less then 20 ns, as this is approximately the duration of the current spike generated during a photon detection [17].
- **Threshold values**: The threshold values of the trigger must match the voltage drop over the quenching resistor when a photon is detected. The exact value for this voltage drop isn't known, as the SPADs being used don't work as they should, but an estimation was made based on the tests we were able to do.

An excess voltage of approximately 3V was selected when validating the SPADs, which sets the maximum expected voltage drop over the quenching resistor. The actually measured voltage over the quenching resistor was slightly lower then 3V, but 3V was used to simplify the measurements. After evaluating available options, we determined that the 74HC14 inverting Schmitt trigger best met our requirements. This is an inverting Schmitt trigger, so a detected photon equals a logic 0 and no detection a logic 1. An inverting trigger was selected as these have a shorter propagation delay when compared to non-inverting Schmitt triggers. A non inverting Schmitt trigger is an inverting Schmitt trigger with an additional not gate. More logic creates a longer propagation delay. Several characteristics of the 74HC14 made us opt for this specific trigger, these characteristics do depend on the supplied voltage V_{cc}:

- **Propagation delay** The delay given in the datasheet is for both pulling the output signal high to low and low to high, so about half of the value is looked at as this needs to be lower then 20ns. The delay is 22ns at V_{cc} = 2V and 7ns at V_{cc} = 4.5V
- **Threshold values**: At V_{cc} = 2V the upper threshold voltage is 1.2V and the lower threshold voltage is 0.5V. At V_{cc} = 4.5V the upper threshold voltage is 2.4V and the lower threshold voltage is 1.4V.

Taking these characteristics into account a supply voltage of 3.3V was selected. At V_{cc} = 3.3V we estimate the upper threshold voltage to be 2V, the lower threshold voltage to be 1.1V and the propagation delay to be 11ns. Table 5.1 summarizes the key parameters of the 74HC14 inverting Schmitt trigger. V_{OH} and V_{OL} are the output voltage when the output signal is high and low respectively.

V_{cc}	V_{up}	V_{low}	t_d	V_{OH}	V_{OL}
3.3V	2V	1.1V	11ns	3.3V	0.1V

Table 5.1: 74HC14 parameters used in ADC

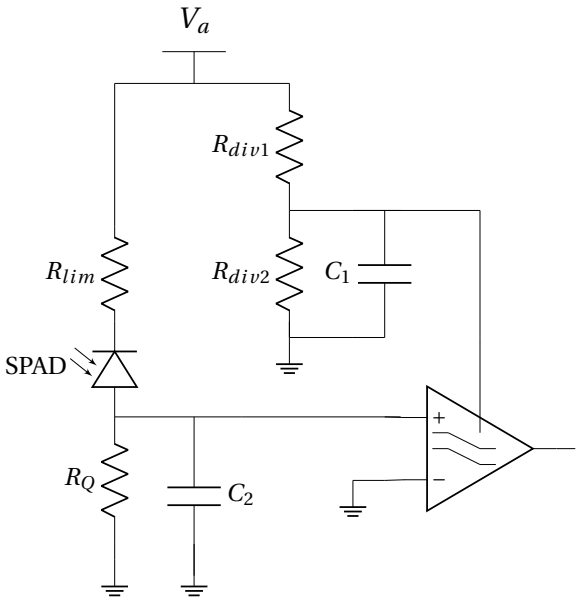

Figure 5.2: Analog to Digital Converter using a Schmitt trigger.

After the Schmitt trigger was selected the rest of the circuit could be designed. Inspiration for this model was taken from a paper on the characterization of SPAD arrays [38]. A voltage divider was used to supply the correct amount of voltage to the trigger. R_{div1} and R_{div2} are used for this. C_1 is there to limit noise contributions. A resistor is also added before the SPAD, R_{lim}, so the amount of current going through the SPAD is controlled. We didn't find any restrictions on the amount of current entering the SPAD, but added the resistor as it wont affect the rest of the circuit. Lastly C_2 was added to make detecting the current spike generated by the SPAD easier to detect. C_2 stores some of the charge accumulated during the avalanche and releasing it when the current is quenched, thereby enlarging the avalanche current and in doing so making voltage drop over the quenching resistor, R_Q, higher for a prolonged amount of time.

5.3. SIMULATIONS

The SPAD themselves can't be simulated directly, therefore a voltage pulse is used to simulate the characteristic voltage spike generated when a photon is absorbed in the SPAD. The pulse will maintain a voltage above 1V for about 20ns, which corresponds to the duration of the detection window of the voltage spike of the SPAD [17]. We tried to model the shape of the voltage spike by having a short rise and on time combined with a longer fall time. To simulate the circuit LTSpice [43], a circuit simulator, was used. LTSpice provides a built-in Schmitt trigger component. The inverting Schmitt trigger component was selected for simulations to match the intended circuit behaviour.

The propagation delay was intentionally set higher then we expected it to be, so if the trigger has a longer propagation delay the circuit will still function as needed. The simulated graphs are shown in Fig. A.7 and Fig. 5.3. Fig. A.7 shows the Schmitt trigger output and the simulated SPAD pulse in ideal circumstance, if there would be no delay. From this graph we can clearly see that the output switches from high to low at 2v and from low to high at 1.1V, all as expected. Fig. 5.3 shows the same graph but then with the propagation delay. The output still switches from high to low and low to high during each SPAD pulse, from which we can conclude that the 74HC14 should work in our circuit.

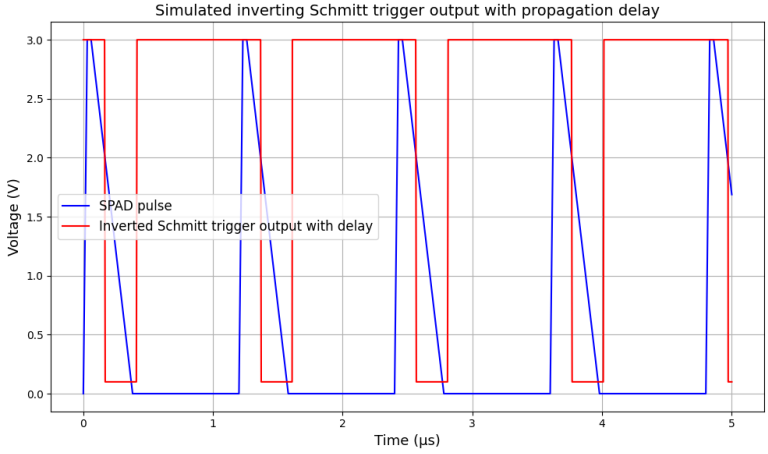

Figure 5.3: Output of inverting Schmitt trigger and simulated SPAD pulse with propagation delay. Output switches with a delay of 15 ns.

5.4. MEASUREMENT SET-UP + TESTS

For testing purposes the SPAD and R_{lim} were replaced with a function generator. To assess Schmitt trigger performance at high frequencies, pulse signals with a width of 30 ns, the generator's shortest possible pulse width, was used. The generator's input waveform and Schmitt trigger output, which was measured over a resistor from the Schmitt triggers' output to ground, were compared to asses the performance of the trigger. V_{cc} was set at 3.3V and a coupling capacitor was added next to the source to make sure voltage is supplied continuously. Fig. 5.4 provides a schematic overview of the measurement set-up.

Throughout several tests we will validate the performance of the Schmitt trigger and its surrounding circuitry. The tests we did are:

1. **Basic trigger operation:** By using a low frequency ramp waveform the initial verification was done. This low frequency, stable, signal shows the threshold voltages and (logic) output voltage levels making it easier to validate them then at high frequencies.

2. **High frequency response:** To evaluate dynamic performance, 30 ns pulses were used. Both the input and output channels' waveforms were distorted by noise, but the trigger still managed to transition correctly.

3. **Propagation delay:** A square wave, with a frequency of 500kHz, was used to measure timing performance. To determine the propagation delay the delay between the rising edge of the input pulse reaching its threshold voltage and the matching falling edge of the output starting to decrease was measured.

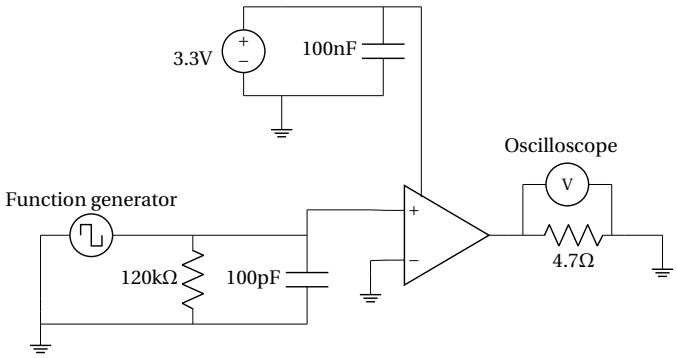

Figure 5.4: Measurement set-up for testing the Schmitt trigger circuit. The function generator simulates the voltage spike of a detected photon. The output will be measured over the resistor after the Schmitt trigger and will be compared versus the signal from the function generator

5.5. RESULTS + CONCLUSION

The Schmitt trigger's hysteretic properties are confirmed by experiment in Fig. 5.5. The device shows:

- **Upper threshold voltage,** V_{up}: 1.96V (high to low transition)
- **Lower threshold voltage,** V_{low}:1.47V (low to high transition)

Notably, the measured V_{low} is 33.6% higher than the expected 1.1 V, most likely as a result of input impedance effects [44] or temperature-dependent leakage currents [45]. On the other hand, this higher threshold increases the noise margin which could improve the accuracy of photon counting.

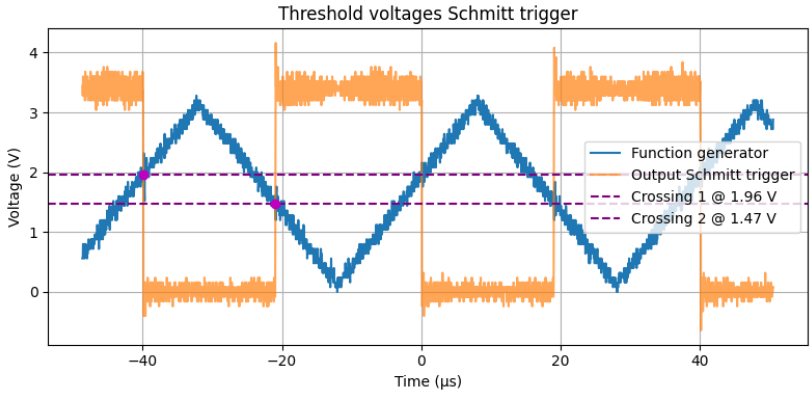

Figure 5.5: Graph highlighting the threshold voltages of the Schmitt trigger. Due to the signal being very noisy there was a deviation in each measurement. The threshold voltages in this segment were 1.96V for pulling the output signal from high to low and 1.47V for pulling the output signal from low to high.

As shown in Fig. 5.6 the trigger maintains functionality under 30 ns pulse excitation even with high frequency noise. Some key observations are:

- High output voltage decreases from 3V to 2.2V
- Low output voltage increases from 0V to 0.6V

This is something to keep in mind when processing the output of the Schmitt trigger to counter or different way to photon count.

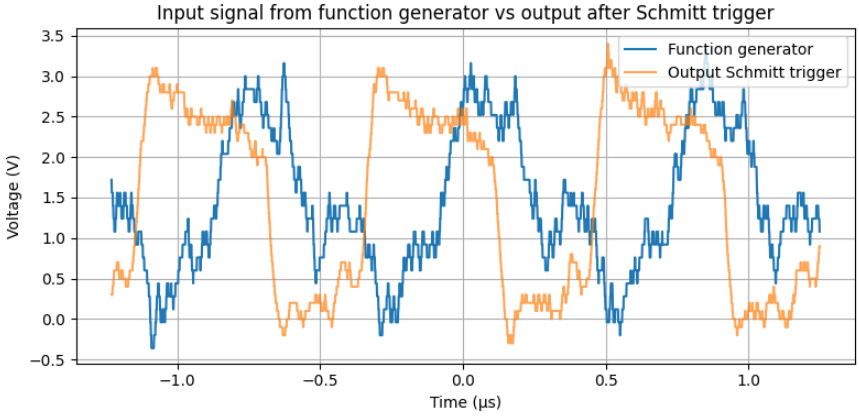

Figure 5.6: Input pulse from function generator with a frequency of 12.5 MHz and a pulse width of 30 ns. Very noisy signal, but the Schmitt trigger output is still correct.

In the last test the propagation delay was measured. Fig. 5.7 shows the graph used to find this delay. A block wave excitation with a frequency of 500kHz was used. The difference between the function generator reaching 2V and the output of the Schmitt trigger

pulling low is what was measured. A value of 21 ns was found. This exceeds the typical 74HC14 propagation delay possibly due to parasitics of the measurement/test set-up. Although this delay limits bandwidth by 47.6 MHz, it still satisfies SPAD dead time requirements which vary up to 100 ns [17]. This is a higher then expected and something to keep in mind when selecting the ADC and its components to implement.

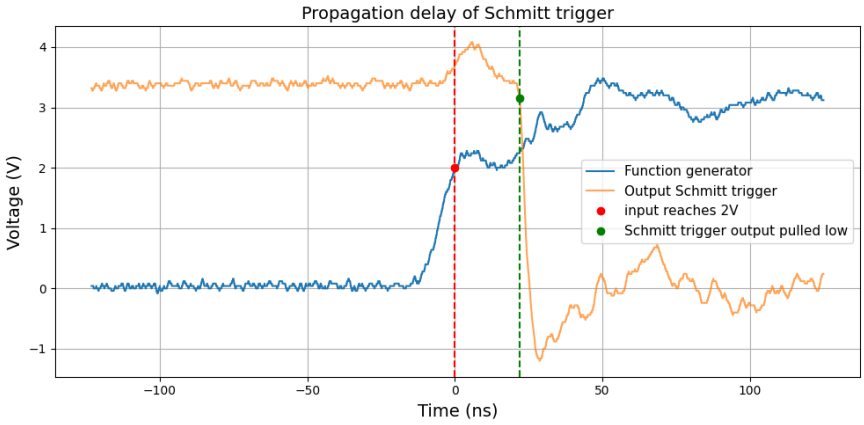

Figure 5.7: Graph highlighting the propagation delay of the Schmitt trigger. The red point marks when the input first reaches 2V and the green point consequently when the Schmitt trigger output is pulled low because of this. The measured propagation delay, from pulling high to low, is 21ns

Based on the tests that were conducted, it can be concluded that the Schmitt trigger is a good option to use for the ADC in combination with the SPAD. Although the measured propagation delay could be a drawback in high-speed applications, it is expected to be controllable within its intended system. The Schmitt trigger's other measured attributes were all either in line with predictions or showed only slight variations, which are anticipated to have only positive impact on the system's overall performance.

6

CONCLUSION AND FUTURE WORK

In conclusion, a 3D SPAD model was successfully created, and its electrical characteristics, which include I-V and C-V curves, were simulated. The basic behavior of the model was validated by the simulations, which showed breakdown voltages in line with common CMOS SPAD operating ranges. However for more accurate results the exact retrograde doping profiles have to be known.
Experimental validation confirmed the diode action of the SPADs, by showing correct breakdown and forward bias voltages, 0.9V and 16.8V respectively, but the SPAD failed to detect photons. This failure is attributed to a critical design flaw: the absence of an N-well between the P+ area and the DNW. Lowering the electric field within the SPAD to the point where it can no longer sustain Geiger mode operation and it continuously conducts current when biased above breakdown voltage rather than photon-triggered avalanches.
For the ADC a new circuit was designed including a Schmitt trigger. The inherent noise immunity of the Schmitt trigger proved especially useful for the high frequency SPAD pulses. The propagation delay was slightly longer then expected (~5ns), but should still work in combination with the voltage pulses from the SPAD.

Future work

The work done during this project provides a good framework for further research into the creation of a fully integrated IC for magnetic biosensing and -imaging. However, several further steps are required for full characterisation and validation of future designs. We recommend the following steps to be taken: *i)* analysis of the SPAD design in TCAD with accurate retrograde doping profiles according to the technology used, *ii)* simulation and analysis of more SPAD characteristics in TCAD, namely the photon detection probability (PDP) vs wavelength, *iii)* simulation of incident photons on the SPAD model in TCAD, *iv)* SPICE simulation of the SPAD with the surrounding circuitry, and *v)* verification and expansion of the ADC circuit using a working SPAD.

A lot of these steps involve TCAD simulations, as there is a lot more that can be done in terms of pre-fabrication device analysis. The most important next step for the TCAD simulations is point *i*. Given the fact that the exact retrograde doping profiles of the TSMC 40nm node were not known when the 3D SPAD models were created, the simulations might show skewed results when compared to the fabricated devices. With more detailed knowledge of the doping profiles, a more thorough analysis can be made of any proposed design. Additionally, this allows the design to be directly matched to any re-

quired specifications. This leads us to point *ii*, where the PDP vs wavelength characteristic can be determined using TCAD. If the PDP of a proposed design is known, the effectivity in detection of the required photon wavelengths can be determined. Ideally, the SPAD should be able to detect all photons emitted by NV centers and no others. Granted, this ideal situation is a long stretch, but the closer the design is able to get to such an ideal situation, the better the accuracy will become.

For point *iii*, simulation of incident photons on the SPAD model, should show if the proposed design will actually be able to detect photons. Verifying that an incident photon will result in an avalanche current is imperative for determining if a proposed design behaves as a SPAD or simply as a diode. Simulating the I-V and C-V characteristics and the PDP will show how the final characteristics of the device will approximately turn out, yet provide no information about any photon detection behaviour. Simulating an incident photon on the SPAD should provide more certainty on the validity of any proposed design. Furthermore, this allows for further simulation of the SPAD with the surrounding circuitry in SPICE, where we reach point *iv*. The sdevice simulation tool allows for SPICE netlists to be simulated in conjunction with the SPAD model. With this, the behaviour of the SPAD when connected with the surrounding circuit can be determined. Alternatively, the SPAD can be modeled in SPICE using only passive components. However, this requires the value of these components to be known. Both options provide their own merits, yet for the most accurate results we suggest simulation using TCAD.

Finally, the ADC design discussed in chapter 5 has not been tested using a SPAD. Instead, the SPAD was mocked up through the use of a function generator. Bringing us to point *v*, and the final point of future work we propose. Mocking up components is a good way to test if other circuit components work or to measure certain characteristics of the circuit. Yet, testing the full circuit and verifying the behaviouro of the fully completed circuit is required as well. This also allows for detection of any undesired behaviour and to account for it in testing.

BIBLIOGRAPHY

[1] Gopalakrishnan Balasubramanian et al. “Nitrogen-Vacancy color center in diamond — emerging nanoscale applications in bioimaging and biosensing”. In: *Current Opinion in Chemical Biology*. Molecular imaging 20 (June 2014), pp. 69–77. ISSN: 1367-5931. DOI: 10.1016/j.cbpa.2014.04.014. URL: https://www.sciencedirect.com/science/article/pii/S1367593114000593.

[2] Alberto Boretti, Lorenzo Rosa, and Stefania Castelletto. “Towards Single Biomolecule Imaging via Optical Nanoscale Magnetic Resonance Imaging”. en. In: *Small* 11.34 (2015), pp. 4229–4236. ISSN: 1613-6829. DOI: 10.1002/smll.201500764. URL: https://onlinelibrary.wiley.com/doi/abs/10.1002/smll.201500764.

[3] David R Glenn et al. “Single-cell magnetic imaging using a quantum diamond microscope”. en. In: *Nature Methods* 12.8 (Aug. 2015), pp. 736–738. ISSN: 1548-7091, 1548-7105. DOI: 10.1038/nmeth.3449. URL: https://www.nature.com/articles/nmeth.3449.

[4] Iris Cusini et al. “Historical Perspectives, State of Art and Research Trends of SPAD Arrays and Their Applications (Part II: SPAD Arrays)”. English. In: *Frontiers in Physics* 10 (July 2022). Publisher: Frontiers. ISSN: 2296-424X. DOI: 10.3389/fphy.2022.906671. URL: https://www.frontiersin.orghttps://www.frontiersin.org/journals/physics/articles/10.3389/fphy.2022.906671/full.

[5] Ester Polo et al. “Magnetic Nanoparticles for Cancer Therapy and Bioimaging”. en. In: *Nanooncology*. ISSN: 2194-0460. Springer, Cham, 2018, pp. 239–279. ISBN: 978-3-319-89878-0. DOI: 10.1007/978-3-319-89878-0_7. URL: https://link.springer.com/chapter/10.1007/978-3-319-89878-0_7.

[6] *Magnetic Activated Cell Sorting: MACS Cell Sorting Protocols*. en. URL: https://www.akadeum.com/technology/macs-magnetic-activated-cell-sorting/ (visited on 06/10/2025).

[7] Suraj Joshy et al. “Accuracy of MRI scan in the diagnosis of ligamentous and chondral pathology in the ankle”. In: *Foot and Ankle Surgery* 16.2 (June 2010), pp. 78–80. ISSN: 1268-7731. DOI: 10.1016/j.fas.2009.05.012. URL: https://www.sciencedirect.com/science/article/pii/S126877310900068X.

[8] Alexander P. S. Kirkham, Mark Emberton, and Clare Allen. “How Good is MRI at Detecting and Characterising Cancer within the Prostate?” In: *European Urology*. European Urology goes Platinum 50.6 (Dec. 2006), pp. 1163–1175. ISSN: 0302-2838. DOI: 10.1016/j.eururo.2006.06.025. URL: https://www.sciencedirect.com/science/article/pii/S0302283806007421.

[9] Lauren Vincent. *Imaging with very few photons: EMCCD, sCMOS, and SPAD Detectors*. en-US. Nov. 2024. URL: https://www.axiomoptics.com/blog/compare-emccd-scmos-spad-technology/ (visited on 06/10/2025).

[10] Kazuhiro Morimoto et al. “Megapixel time-gated SPAD image sensor for 2D and 3D imaging applications”. EN. In: *Optica* 7.4 (Apr. 2020). Publisher: Optica Publishing Group, pp. 346–354. ISSN: 2334-2536. DOI: 10.1364/OPTICA.386574. URL: https://opg.optica.org/optica/abstract.cfm?uri=optica-7-4-346.

[11] K. Morimoto et al. “3.2 Megapixel 3D-Stacked Charge Focusing SPAD for Low-Light Imaging and Depth Sensing”. In: *2021 IEEE International Electron Devices Meeting (IEDM)*. ISSN: 2156-017X. Dec. 2021, pp. 20.2.1–20.2.4. DOI: 10.1109/IEDM19574.2021.9720605. URL: https://ieeexplore.ieee.org/abstract/document/9720605.

[12] Dylan Aliberti. “Characterization of Single Photon Avalanche Diodes and Integration with Diamond for Quantum Biosensing”. MA thesis. Delft University of Technology, 2024. URL: https://resolver.tudelft.nl/uuid:52304668-612d-45ea-8f16-fba2003b0c46.

[13] Sander Britton, Martijn Janssen, and Eva Nootenboom. *Single-Photon Avalanche Diodes (SPAD) for Quantum Sensors*. en. BSc Thesis. 2023. URL: https://resolver.tudelft.nl/uuid:70495d7c-16b0-4939-979a-01ce16768380.

[14] F. Zappa et al. “SPICE modeling of single photon avalanche diodes”. In: *Sensors and Actuators A: Physical* 153.2 (Aug. 2009), pp. 197–204. ISSN: 0924-4247. DOI: 10.1016/j.sna.2009.05.007. URL: https://www.sciencedirect.com/science/article/pii/S0924424709002581.

[15] Iris Cusini et al. “Historical Perspectives, State of art and Research Trends of Single Photon Avalanche Diodes and Their Applications (Part 1: Single Pixels)”. English. In: *Frontiers in Physics* 10 (June 2022). Publisher: Frontiers. ISSN: 2296-424X. DOI: 10.3389/fphy.2022.906675. URL: https://www.frontiersin.orghttps://www.frontiersin.org/journals/physics/articles/10.3389/fphy.2022.906675/full.

[16] Virginia Spanoudaki and Craig Levin. “Photo-Detectors for Time of Flight Positron Emission Tomography (ToF-PET)”. In: *Sensors* 10 (Nov. 2010), pp. 10484–10505. DOI: 10.3390/s101110484.

[17] S. Cova et al. “Avalanche photodiodes and quenching circuits for single-photon detection”. EN. In: *Applied Optics* 35.12 (Apr. 1996). Publisher: Optica Publishing Group, pp. 1956–1976. ISSN: 2155-3165. DOI: 10.1364/AO.35.001956. URL: https://opg.optica.org/ao/abstract.cfm?uri=ao-35-12-1956.

[18] Ion Vornicu et al. “Compact CMOS active quenching/recharge circuit for SPAD arrays”. en. In: *International Journal of Circuit Theory and Applications* 44.4 (2016), pp. 917–928. ISSN: 1097-007X. DOI: 10.1002/cta.2113. URL: https://onlinelibrary.wiley.com/doi/abs/10.1002/cta.2113.

[19] Danilo Bronzi. “Front-side and back-side illuminated spad arrays for 2D imaging and 3D ranging”. PhD thesis. Politecnico Di Milano, Nov. 2014. DOI: 10.13140/RG.2.1.3329.9047/1.

[20] J.L. Sánchez Toural et al. “Diamond-defect engineering of NV-centers using ion beam irradiation”. In: *Diamond and Related Materials* 151 (2025), p. 111838. ISSN: 0925-9635. DOI: https://doi.org/10.1016/j.diamond.2024.111838. URL: https://www.sciencedirect.com/science/article/pii/S0925963524010513.

[21] “Fundamentals of magnetic field measurement with NV centers in diamond”. English. In: *Qnami* (Dec. 2020). URL: https://qnami.ch/wp-content/uploads/2020/12/2020-12-07-Qnami-TN1-The-NV-center-1.pdf (visited on 04/30/2025).

[22] David A. Hopper, Henry J. Shulevitz, and Lee C. Bassett. “Spin Readout Techniques of the Nitrogen-Vacancy Center in Diamond”. In: *Micromachines* 9.9 (2018). ISSN: 2072-666X. DOI: 10.3390/mi9090437. URL: https://www.mdpi.com/2072-666X/9/9/437.

[23] Marcus W. Doherty et al. “The nitrogen-vacancy colour centre in diamond”. In: *Physics Reports* 528.1 (2013). The nitrogen-vacancy colour centre in diamond, pp. 1–45. ISSN: 0370-1573. DOI: https://doi.org/10.1016/j.physrep.2013.02.001. URL: https://www.sciencedirect.com/science/article/pii/S0370157313000562.

[24] Nicholas R. Jungwirth. “Spin and Charge Dynamics of Nitrogen-Vacancy Centers in Diamond”. PhD thesis. University of California, Santa Barbara, 2020. URL: https://escholarship.org/uc/item/1rj4p2ch.

[25] Zhiying Song et al. “Enhancing fluorescence of diamond NV-centers for quantum sensing: A multi-layer optical antireflection coating”. In: *Diamond and Related Materials* 141 (2024), p. 110584. ISSN: 0925-9635. DOI: https://doi.org/10.1016/j.diamond.2023.110584. URL: https://www.sciencedirect.com/science/article/pii/S0925963523009093.

[26] ETH Zurich. *Zeeman*. en. URL: https://epr.ethz.ch/education/basic-concepts-of-epr/one-elect--in-the-magn--field/zeeman.html (visited on 05/12/2025).

[27] Synopsys. *Synopsys TCAD, Unleash the Power of Smart Technology Modeling - from Atoms to Circuits*. URL: https://www.synopsys.com/manufacturing/tcad.html.

[28] Samantha van Rijs, Lars Visser, and Dagmar Westenbrink. *On-chip SPAD array with IO designed for quantum sensing*. en. BSc Thesis. 2023. URL: https://resolver.tudelft.nl/uuid:d6644989-1269-45b0-bed1-70e7640c4c00.

[29] Matteo Perenzoni, Lucio Pancheri, and David Stoppa. “Compact SPAD-Based Pixel Architectures for Time-Resolved Image Sensors”. en. In: *Sensors* 16.5 (May 2016), p. 745. ISSN: 1424-8220. DOI: 10.3390/s16050745. URL: https://www.mdpi.com/1424-8220/16/5/745.

[30] TSMC. *TSMC 40nm CMOS node*. 2016. URL: https://www.tsmc.com/english/dedicatedFoundry/technology/logic/l_40nm (visited on 06/10/2025).

[31] Behzad Razavi. *Design of analog CMOS integrated circuits*. en. Second edition. New York, NY: McGraw-Hill Education, 2017. ISBN: 978-0-07-252493-2 978-981-4636-26-1.

[32] Synopsys. *Sentaurus™ Structure Editor User Guide*. en. 2017. URL: https://tinyurl.com/584pajvh (visited on 06/04/2025).

[33] Synopsys. *Sentaurus™ Device User Guide*. en. 2015. URL: https://www.google.com/url?sa=t&source=web&rct=j&opi=89978449&url=https://www.researchgate.net/profile/Nabil-Ashraf/post/How-to-control-the-slope-of-output-characteristicsId-Vd-of-a-GAA-nanowire-FET-which-shows-flat-saturated-region/attachment/5de3c15bcfe4a777d4f64432/AS%253A831293646458882%25401575207258619/download/Synopsis%5C_Sentaurus%5C_user%5C_manual.pdf&ved=2ahUKEwijh57fh9iNAxVW8LsIHRdiPEMQFnoECCsusg=AOvVaw2oaNOXzwsFeJNfW7okeisG (visited on 06/04/2025).

[34] R. Van Overstraeten and H. De Man. "Measurement of the ionization rates in diffused silicon *p-n* junctions". In: *Solid-State Electronics* 13.5 (May 1970), pp. 583–608. ISSN: 0038-1101. DOI: 10.1016/0038-1101(70)90139-5. URL: https://www.sciencedirect.com/science/article/pii/0038110170901395.

[35] W. Shockley and W. T. Read. "Statistics of the Recombinations of Holes and Electrons". In: *Physical Review* 87.5 (Sept. 1952). Publisher: American Physical Society, pp. 835–842. DOI: 10.1103/PhysRev.87.835. URL: https://link.aps.org/doi/10.1103/PhysRev.87.835.

[36] Fahrettin Sarcan et al. "Negative capacitance in a novel bidirectional p-i-n diode for near-infrared LED and photodetector applications". In: *Optics & Laser Technology* 190 (Nov. 2025), p. 113207. ISSN: 0030-3992. DOI: 10.1016/j.optlastec.2025.113207. URL: https://www.sciencedirect.com/science/article/pii/S0030399225007984 (visited on 06/09/2025).

[37] Dr Alistair Sproul. "Understanding the p-n Junction". en. In: ().

[38] Hesong Xu et al. "Design and characterization of a p+/n-well SPAD array in 150nm CMOS process". EN. In: *Optics Express* 25.11 (May 2017). Publisher: Optica Publishing Group, pp. 12765–12778. ISSN: 1094-4087. DOI: 10.1364/OE.25.012765. URL: https://opg.optica.org/oe/abstract.cfm?uri=oe-25-11-12765.

[39] F. Zappa et al. "Principles and features of single-photon avalanche diode arrays". en. In: *Sensors and Actuators A: Physical* 140.1 (Oct. 2007), pp. 103–112. ISSN: 09244247. DOI: 10.1016/j.sna.2007.06.021. URL: https://linkinghub.elsevier.com/retrieve/pii/S0924424707004967.

[40] editor. *Comparators*. en-GB. Apr. 2018. URL: https://www.student-circuit.com/learning/year2/measurements-and-tools/difference-between-comparator-and-schmitt-trigger/.

[41] *Schmitt Trigger Hysteresis Provides Noise-free Switching and Output*. en-US. Jan. 2021. URL: https://resources.pcb.cadence.com/blog/2021-schmitt-trigger-hysteresis-provides-noise-free-switching-and-output.

[42] Abhishek Singh. *Schmitt Trigger Circuit Working and Applications*. English. Dec. 2020. URL: https://hackatronic.com/schmitt-trigger-circuit-working-and-applications/.

[43] *Download LTspice | Analog Devices*. URL: https://www.analog.com/en/resources/design-tools-and-calculators/ltspice-simulator.html (visited on 06/15/2025).

[44] HTC Korea. *CMOS Quad 2-Input NAND Schmitt Triggers CD4093B*. Datasheet. 2002. URL: https://datasheetspdf.com/pdf-file/135970/HTC/CD4093B/1.

[45] Texas Instruments. *SN74HC14 Hex Inverters with Schmitt-Trigger Inputs*. Datasheet, Rev. L. 2025. URL: https://www.ti.com/lit/gpn/sn74hc14.

A

APPENDIX A - ADDITIONAL FIGURES AND GRAPHS

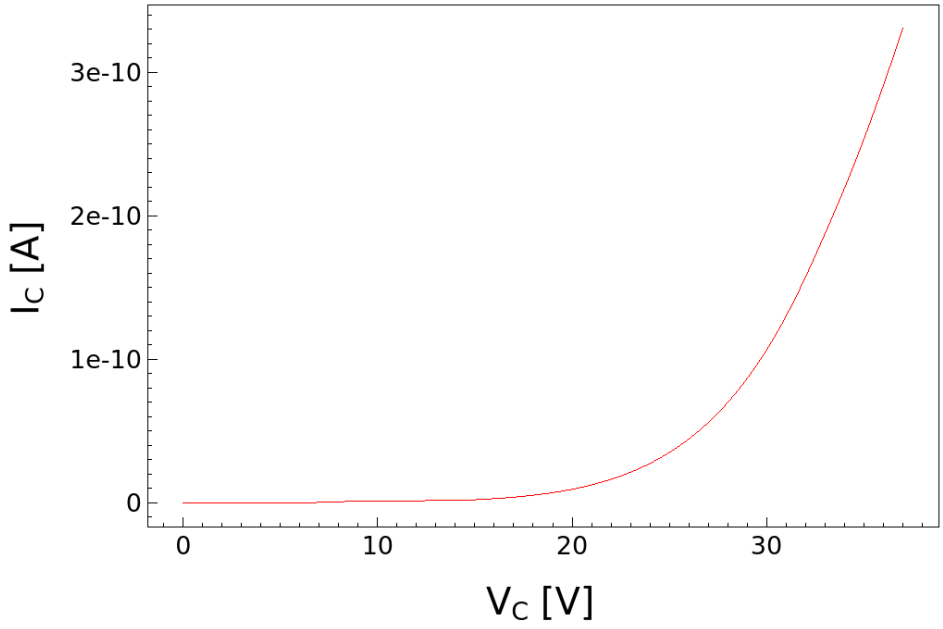

Figure A.1: I-V curve for the octagonal SPAD with analytic doping profiles and STI regions included

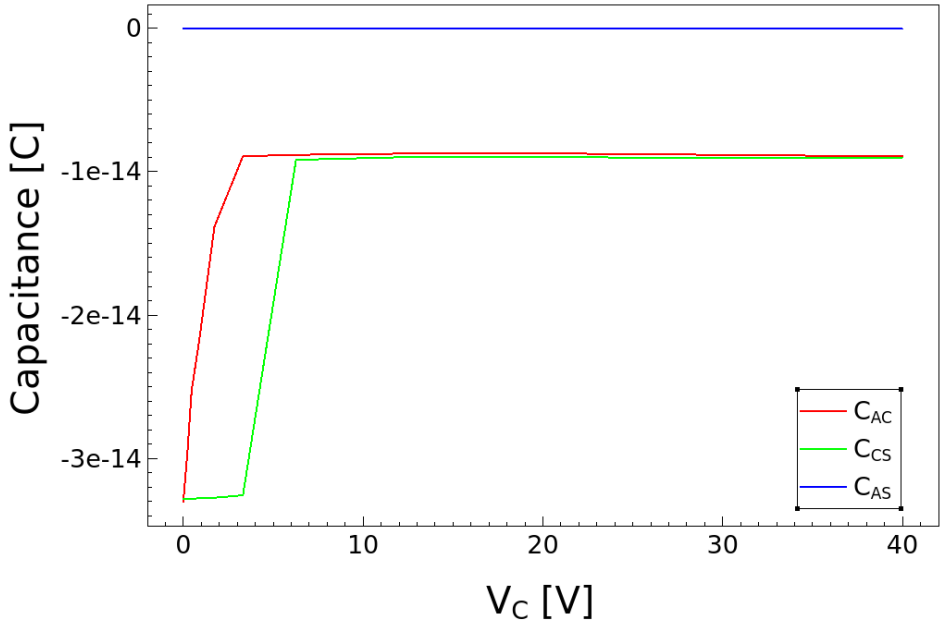

Figure A.2: C-V curve for the octagonal SPAD with constant doping profiles

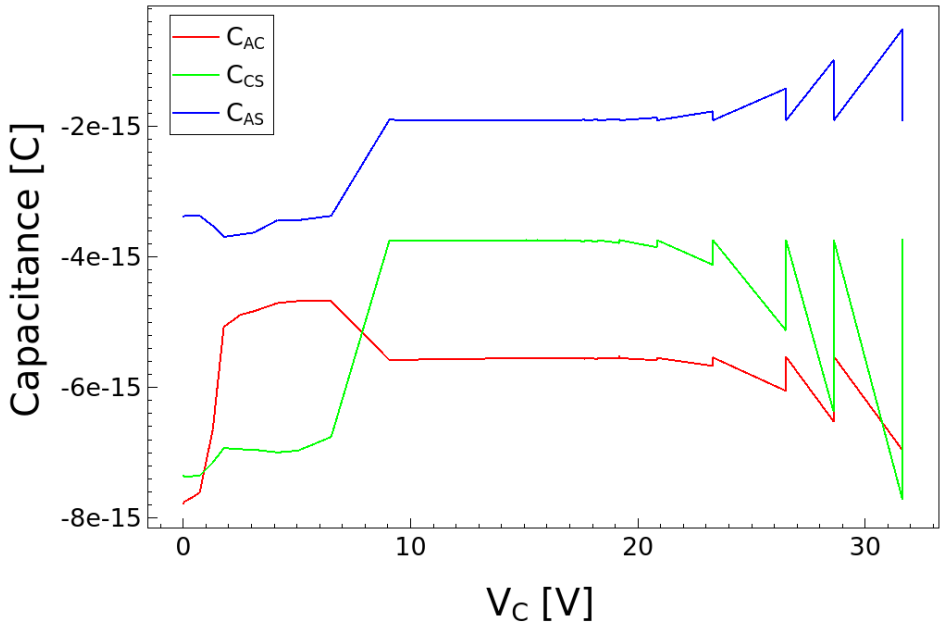

Figure A.3: C-V curve for the octagonal SPAD with analytic doping profiles and STI regions included

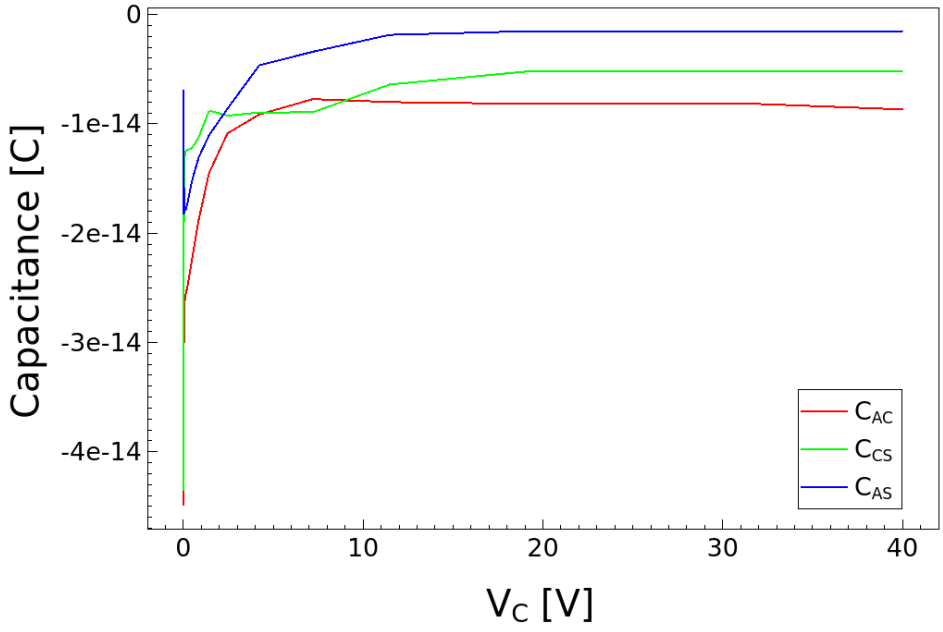

Figure A.4: C-V curve for the rectangular SPAD with constant doping profiles

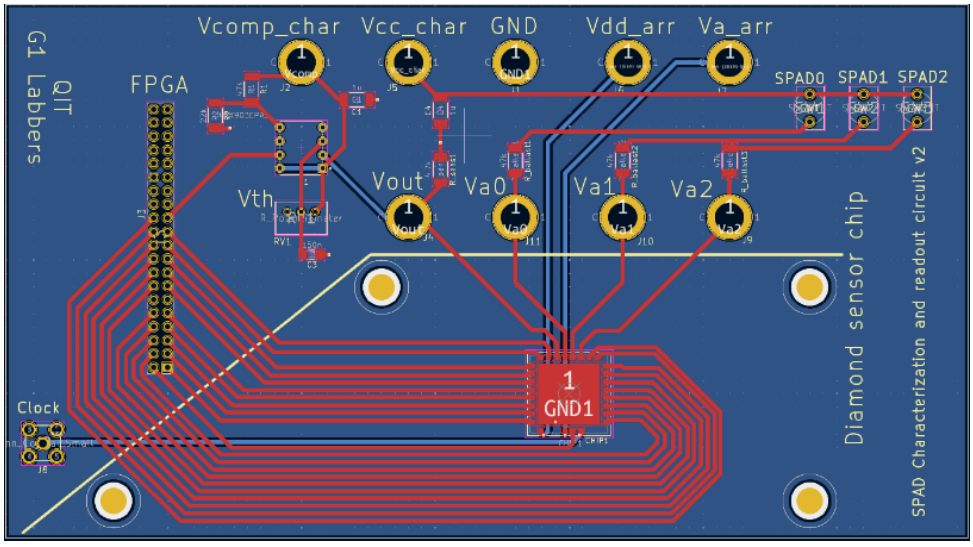

Figure A.5: The PCB design, created in KiCad. The PCB includes connectors to connect the FPGA and power to the chip, as well as a SPAD characterization circuit. The chip is mounted and wirebonded upon this PCB. Taken from Aliberti [12]

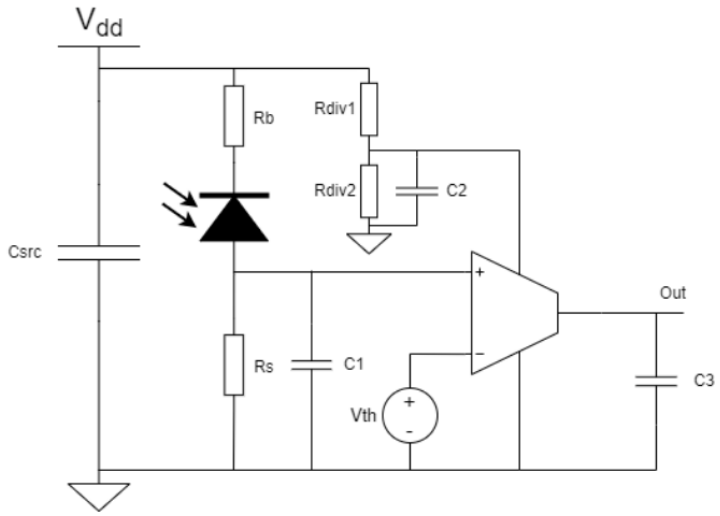

Figure A.6: Schematic representation of ADC designed in 2023. Taken from Britton et al. [13]

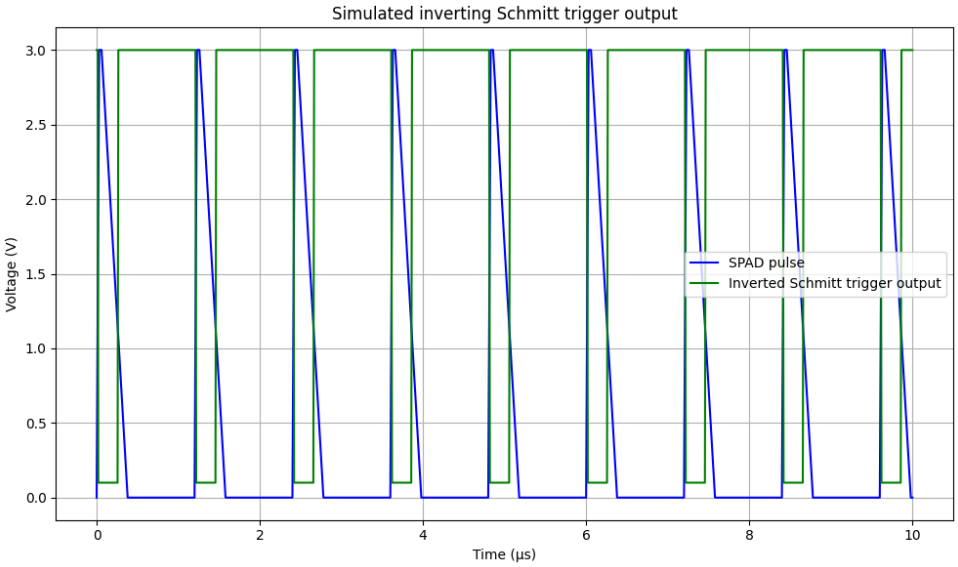

Figure A.7: Output of inverting Schmitt trigger and simulated SPAD pulse without propation delay. output switchs from high to low at 2V and from low to high at 1.1V

B

APPENDIX B - TCAD SENTAURUS COMMAND FILES

The following command file texts can also be found in this Github repo (https://github.com/TheKnight1993/BSc_Thesis_TCAD_cmd_files).

B.1. SENTAURUS STRUCTURE EDITOR COMMAND FILES

B.1.1. RECTANGULAR SPAD

Constant doping profiles

```
; Initialise workspace
(sde:clear)

; Create substrate doped regions
(sdegeo:create-polygon (list
        (position 0 0 0)
        (position 0 -12 0)
        (position -8.5 -12 0)
        (position -8.5 -11 0)
        (position -7 -11 0)
        (position -7 -10 0)
        (position -4 -10 0)
        (position -4 0 0)
        (position 0 0 0)
        )
        "Silicon"
        "Substrate_1"
)

(sdegeo:create-polygon (list
        (position -7 0 0)
        (position -7 -9 0)
        (position -8.5 -9 0)
        (position -8.5 -8 0)
        (position -10 -8 0)
        (position -10 -7 0)
```

```
        (position -8.5 -7 0)
        (position -8.5 0 0)
        (position -7 0 0)
        )
        "Silicon"
        "Substrate_2"
)

; Create process doped regions
(sdegeo:create-rectangle (position -4 0 0) (position -7 -10 0) "
    ↪ Silicon" "DNW")
(sdegeo:create-rectangle (position -7 -9 0) (position -8.5 -11 0) "
    ↪ Silicon" "NW")
(sdegeo:create-rectangle (position -8.5 -8 0) (position -10 -12 0) "
    ↪ PolySi" "NP")
(sdegeo:create-rectangle (position -8.5 0 0) (position -10 -7 0) "
    ↪ PolySi" "PP")

; Create oxide layers
(sdegeo:create-rectangle (position -10 -6 0) (position -11 -9.5 0) "
    ↪ Oxide" "Ox")
(sdegeo:create-rectangle (position -10 -10.5 0) (position -11 -12 0)
    ↪ "Oxide" "Ox")

; Define contacts for simulation
(sdegeo:set-contact (find-edge-id (position -10 -2 0)) "anode")
(sdegeo:set-contact (find-edge-id (position -10 -10.2 0)) "cathode")
(sdegeo:set-contact (find-edge-id (position 0 -2 0)) "bulk")

; Create a sweeping path and sweep along it
(define rectangular_path (sdegeo:create-polyline-wire (list
        (position 0 6 0)
        (position 0 6 6)
        (position 0 -6 6)
        (position 0 -6 -6)
        (position 0 6 -6)
        (position 0 6 0)
)))
(sdegeo:sweep (entity:faces (find-material-id "PolySi"))
    ↪ rectangular_path
  (sweep:options "solid" #t "rigid" #f "miter_type" "default" ))
(sdegeo:sweep (entity:faces (find-material-id "Silicon"))
    ↪ rectangular_path
  (sweep:options "solid" #t "rigid" #f "miter_type" "default" ))
(sdegeo:sweep (entity:faces (find-material-id "Oxide"))
```

```
    ↪ rectangular_path
  (sweep:options "solid" #t "rigid" #f "miter_type" "default" ))

; Define and set doping profiles
(sdedr:define-constant-profile "NP_doping" "
    ↪ PhosphorusActiveConcentration" 1e+21)
(sdedr:define-constant-profile "DNW_doping" "
    ↪ PhosphorusActiveConcentration" 1e+19)
(sdedr:define-constant-profile "NW_doping" "
    ↪ PhosphorusActiveConcentration" 1e+15)
(sdedr:define-constant-profile "Substrate_doping" "
    ↪ BoronActiveConcentration" 1e+15)
(sdedr:define-constant-profile "PP_doping" "BoronActiveConcentration"
    ↪  1e+21)

(sdedr:define-constant-profile-material "Substrate_1_doping" "
    ↪ Substrate_doping" "Silicon")
(sdedr:define-constant-profile-material "Substrate_2_doping" "
    ↪ Substrate_doping" "PolySi")
(sdedr:define-constant-profile-region "NP_doping" "NP_doping" "NP")
(sdedr:define-constant-profile-region "DNW_doping" "DNW_doping" "DNW
    ↪ ")
(sdedr:define-constant-profile-region "NW_doping" "NW_doping" "NW")
(sdedr:define-constant-profile-region "PP_doping" "PP_doping" "PP")

; Define meshing strategy
(sdedr:define-refinement-size "RefDef.Mat.All" 5 5 5 0.5 0.5 0.5)
(sdedr:define-refinement-placement "Ref.Mat.All" "RefDef.Mat.All" (
    ↪ list "material" "Silicon" "material" "PolySi"))
(sdedr:define-refinement-function "RefDef.Mat.All" "
    ↪ DopingConcentration" "MaxTransDiff" 0.05)
(sdedr:define-refinement-function "RefDef.Mat.All" "MaxLenInt" "
    ↪ Silicon" "PolySi" 0.5 1.4)
(sdedr:define-refinement-function "RefDef.Mat.All" "MaxLenInt" "
    ↪ Silicon" "Silicon" 0.5 1.4)

; Mesh the device
(sde:build-mesh "n1")
(system:command "svisual n1_msh.tdr &")
```

Analytic doping profiles

```
; Rectangular SPAD
; Initialise workspace
(sde:clear)
```

```
; Create substrate doped regions
(sdegeo:create-polygon (list
        (position 0 0 0)
        (position 0 -12 0)
        (position -8.5 -12 0)
        (position -8.5 -11 0)
        (position -7 -11 0)
        (position -7 -10 0)
        (position -4 -10 0)
        (position -4 0 0)
        (position 0 0 0)
        )
        "Silicon"
        "Substrate_1"
)

(sdegeo:create-polygon (list
        (position -7 0 0)
        (position -7 -9 0)
        (position -8.5 -9 0)
        (position -8.5 -8 0)
        (position -10 -8 0)
        (position -10 -7 0)
        (position -8.5 -7 0)
        (position -8.5 0 0)
        (position -7 0 0)
        )
        "Silicon"
        "Substrate_2"
)

; Create process doped regions
(sdegeo:create-rectangle (position -4 0 0) (position -7 -10 0) "
    ↪ Silicon" "DNW")
(sdegeo:create-rectangle (position -7 -9 0) (position -8.5 -11 0) "
    ↪ Silicon" "NW")
(sdegeo:create-rectangle (position -8.5 -8 0) (position -10 -12 0) "
    ↪ PolySi" "NP")
(sdegeo:create-rectangle (position -8.5 0 0) (position -10 -7 0) "
    ↪ PolySi" "PP")

; Create oxide layers
(sdegeo:create-rectangle (position -10 -6 0) (position -11 -9.5 0) "
    ↪ Oxide" "Ox")
```

```
(sdegeo:create-rectangle (position -10 -10.5 0) (position -11 -12 0)
    ↪ "Oxide" "Ox")

; Define contacts for simulation
(sdegeo:set-contact (find-edge-id (position -10 -2 0)) "anode")
(sdegeo:set-contact (find-edge-id (position -10 -10.2 0)) "cathode")
(sdegeo:set-contact (find-edge-id (position 0 -2 0)) "bulk")

; Create a sweeping path and sweep along it
(define rectangular_path (sdegeo:create-polyline-wire (list
       (position 0 6 0)
       (position 0 6 6)
       (position 0 -6 6)
       (position 0 -6 -6)
       (position 0 6 -6)
       (position 0 6 0)
)))
(sdegeo:sweep (entity:faces (find-material-id "PolySi"))
    ↪ rectangular_path
  (sweep:options "solid" #t "rigid" #f "miter_type" "default" ))
(sdegeo:sweep (entity:faces (find-material-id "Silicon"))
    ↪ rectangular_path
  (sweep:options "solid" #t "rigid" #f "miter_type" "default" ))
(sdegeo:sweep (entity:faces (find-material-id "Oxide"))
    ↪ rectangular_path
  (sweep:options "solid" #t "rigid" #f "miter_type" "default" ))


; Define and set constant doping profiles
(sdedr:define-constant-profile "Substrate_doping" "
    ↪ BoronActiveConcentration" 1e+15)

(sdedr:define-constant-profile-material "Substrate_doping" "
    ↪ Substrate_doping" "Silicon")
(sdedr:define-constant-profile-material "Substrate2_doping" "
    ↪ Substrate_doping" "PolySi")

; Set BaseLine definitions for analytical profiles
(sdedr:define-refeval-window "BaseLine.DNW" "Rectangle"
       (position -7 -9.8 -9.8)
       (position -7 9.8 9.8))
(sdedr:define-refeval-window "BaseLine.NW" "Polygon" (list
       (position -10 -10.8 -10.8)
       (position -10 -10.8 10.8)
       (position -10 10.8 10.8)
```

```
        (position -10 10.8 -10.8)
        (position -10 -9.2 -10.8)
        (position -10 -9.2 -9.2)
        (position -10 9.2 -9.2)
        (position -10 9.2 9.2)
        (position -10 -9.2 9.2)
        (position -10 -9.21 -10.8)))
(sedr:define-refeval-window "BaseLine.NP" "Polygon" (list
        (position -10 -11.8 -11.8)
        (position -10 -11.8 11.8)
        (position -10 11.8 11.8)
        (position -10 11.8 -11.8)
        (position -10 -8.2 -11.8)
        (position -10 -8.2 -8.2)
        (position -10 8.2 -8.2)
        (position -10 8.2 8.2)
        (position -10 -8.2 8.2)
        (position -10 -8.21 -11.8)))
(sedr:define-refeval-window "BaseLine.PP" "Rectangle"
        (position -10 -6.8 -6.8)
        (position -10 6.8 6.8))

; Define analytical doping profiles
(sedr:define-gaussian-profile "Gauss.DNW"
        "PhosphorusActiveConcentration" "PeakPos" 1.5 "PeakVal" 7.5
            ↪ e19
        "ValueAtDepth" 3e14 "Depth" 2.5 "Gauss" "Factor" 0.5)
(sedr:define-gaussian-profile "Gauss.NW"
        "PhosphorusActiveConcentration" "PeakPos" 1.5 "PeakVal" 1e16
        "ValueAtDepth" 3e14 "Depth" 0.4 "Gauss" "Factor" 0.5)
(sedr:define-gaussian-profile "Gauss.NP"
        "PhosphorusActiveConcentration" "PeakPos" 0 "PeakVal" 5e21
        "ValueAtDepth" 3e19 "Depth" 0.7 "Gauss" "Factor" 0.2)
(sedr:define-gaussian-profile "Gauss.PP"
        "BoronActiveConcentration" "PeakPos" 0 "PeakVal" 5e21
        "ValueAtDepth" 3e19 "Depth" 0.7 "Gauss" "Factor" 0.3)

; Set analytical doping profiles
(sedr:define-analytical-profile-placement "PlaceAP.DNW"
        "Gauss.DNW" "BaseLine.DNW" "Positive" "NoReplace" "Eval")
(sedr:define-analytical-profile-placement "PlaceAP.NW"
        "Gauss.NW" "BaseLine.NW" "Negative" "NoReplace" "Eval")
(sedr:define-analytical-profile-placement "PlaceAP.NP"
        "Gauss.NP" "BaseLine.NP" "Negative" "NoReplace" "Eval")
(sedr:define-analytical-profile-placement "PlaceAP.PP"
```

```
        "Gauss.PP" "BaseLine.PP" "Positive" "NoReplace" "Eval")

; Define meshing strategy
(sedr:define-refinement-size "RefDef.Mat.All" 5 5 5 0.5 0.5 0.5)
(sedr:define-refinement-placement "Ref.Mat.All" "RefDef.Mat.All" (
    ↪ list "material" "Silicon" "material" "PolySi"))
(sedr:define-refinement-function "RefDef.Mat.All" "
    ↪ DopingConcentration" "MaxTransDiff" 0.05)
(sedr:define-refinement-function "RefDef.Mat.All" "MaxLenInt" "
    ↪ Silicon" "PolySi" 0.5 1.4)
(sedr:define-refinement-function "RefDef.Mat.All" "MaxLenInt" "
    ↪ Silicon" "Silicon" 0.5 1.4)

; Mesh the device
(sde:build-mesh "n1")
(system:command "svisual n1_msh.tdr &")
```

B.1.2. OCTAGONAL SPAD

Constant doping profiles

```
; Initialise workspace
(sde:clear)

; Create substrate doped regions
(sdegeo:create-rectangle (position 0 0 0) (position -4 -12 0) "
    ↪ Silicon" "Substrate_1")
(sdegeo:create-polygon (list
        (position -7 -6.6 0)
        (position -7 -8.4 0)
        (position -10 -8.4 0)
        (position -10 -7.2 0)
        (position -8.5 -7.2 0)
        (position -8.5 -6.6 0)
        (position -7 -6.6 0)
        )
        "Silicon"
        "Substrate_2"
)

; Create process doped regions
(sdegeo:create-rectangle (position -4 0 0) (position -7 -12 0) "
    ↪ Silicon" "DNW")
(sdegeo:create-rectangle (position -7 0 0) (position -8.5 -6.6 0) "
    ↪ Silicon" "NW_1")
(sdegeo:create-rectangle (position -7 -8.4 0) (position -8.5 -12 0) "
```

```
    ↪ Silicon" "NW_2.1")
(sdegeo:create-rectangle (position -8.5 -8.4 0) (position -10 -9 0) "
    ↪ Silicon" "NW_2.2")
(sdegeo:create-rectangle (position -8.5 -11.4 0) (position -10 -12 0)
    ↪  "Silicon" "NW_2.3")
(sdegeo:create-rectangle (position -8.5 -9 0) (position -10 -11.4 0)
    ↪ "PolySi" "NP")
(sdegeo:create-rectangle (position -8.5 0 0) (position -10 -7.2 0) "
    ↪ PolySi" "PP")

; Set oxide regions for insulation
(sdegeo:create-rectangle (position -10 -12 0) (position -11 -10.8 0)
    ↪ "Oxide" "Ox")
(sdegeo:create-rectangle (position -10 -9.6 0) (position -11 -6 0) "
    ↪ Oxide" "Ox")

; Define contacts for simulation
(sdegeo:set-contact (find-edge-id (position -10 -2 0)) "anode")
(sdegeo:set-contact (find-edge-id (position -10 -10.2 0)) "cathode")
(sdegeo:set-contact (find-face-id (position 0 2 0)) "bulk")

; Create a sweeping path and sweep along it
(define rectangular_path (sdegeo:create-polyline-wire (list
       (position 0 -6 0)
       (position 0 -6 2.5)
       (position 0 -2.5 6)
       (position 0 2.5 6)
       (position 0 6 2.5)
       (position 0 6 -2.5)
       (position 0 2.5 -6)
       (position 0 -2.5 -6)
       (position 0 -6 -2.5)
       (position 0 -6 0)
)))
(sdegeo:sweep (entity:faces (find-material-id "PolySi"))
    ↪ rectangular_path
  (sweep:options "solid" #t "rigid" #f "miter_type" "default" ))
(sdegeo:sweep (entity:faces (find-material-id "Silicon"))
    ↪ rectangular_path
  (sweep:options "solid" #t "rigid" #f "miter_type" "default" ))
(sdegeo:sweep (entity:faces (find-material-id "Oxide"))
    ↪ rectangular_path
  (sweep:options "solid" #t "rigid" #f "miter_type" "default" ))

; Define contacts for simulation
```

```
(sdegeo:set-contact (find-face-id (position -10 -2 0)) "anode")
(sdegeo:set-contact (find-face-id (position -10 2 0)) "anode")
(sdegeo:set-contact (find-face-id (position -10 0 -2)) "anode")
(sdegeo:set-contact (find-face-id (position -10 0 2)) "anode")
(sdegeo:set-contact (find-face-id (position 0 -2 0)) "bulk")
(sdegeo:set-contact (find-face-id (position 0 -2 2)) "bulk")
(sdegeo:set-contact (find-face-id (position 0 -2 -2)) "bulk")
(sdegeo:set-contact (find-face-id (position 0 0 -2)) "bulk")
(sdegeo:set-contact (find-face-id (position 0 2 -2)) "bulk")
(sdegeo:set-contact (find-face-id (position 0 -2 -2)) "bulk")
(sdegeo:set-contact (find-face-id (position 0 2 0)) "bulk")
(sdegeo:set-contact (find-face-id (position 0 2 2)) "bulk")
(sdegeo:set-contact (find-face-id (position 0 0 2)) "bulk")

; Define and set doping profiles
(sdedr:define-constant-profile "NP_doping" "
    ↪ PhosphorusActiveConcentration" 1e+21)
(sdedr:define-constant-profile "DNW_doping" "
    ↪ PhosphorusActiveConcentration" 1e+19)
(sdedr:define-constant-profile "NW_doping" "
    ↪ PhosphorusActiveConcentration" 1e+15)
(sdedr:define-constant-profile "Substrate_doping" "
    ↪ BoronActiveConcentration" 1e+15)
(sdedr:define-constant-profile "PP_doping" "BoronActiveConcentration"
    ↪  1e+21)

(sdedr:define-constant-profile-material "Substrate_doping" "
    ↪ Substrate_doping" "Silicon")
(sdedr:define-constant-profile-material "Substrate2_doping" "
    ↪ Substrate_doping" "PolySi")
(sdedr:define-constant-profile-region "NP_doping" "NP_doping" "NP")
(sdedr:define-constant-profile-region "DNW_doping" "DNW_doping" "DNW
    ↪ ")
(sdedr:define-constant-profile-region "NW_1_doping" "NW_doping" "NW_1
    ↪ ")
(sdedr:define-constant-profile-region "NW_2.1_doping" "NW_doping" "
    ↪ NW_2.1")
(sdedr:define-constant-profile-region "NW_2.2_doping" "NW_doping" "
    ↪ NW_2.2")
(sdedr:define-constant-profile-region "NW_2.3_doping" "NW_doping" "
    ↪ NW_2.3")
(sdedr:define-constant-profile-region "PP_doping" "PP_doping" "PP")

; Define meshing strategy
(sdedr:define-refinement-size "RefDef.Mat.All" 5 5 5 0.5 0.5 0.5)
```

```
(sdedr:define-refinement-placement "Ref.Mat.All" "RefDef.Mat.All" (
    ↪ list "material" "Silicon" "material" "PolySi"))
(sdedr:define-refinement-function "RefDef.Mat.All" "
    ↪ DopingConcentration" "MaxTransDiff" 0.05)
(sdedr:define-refinement-function "RefDef.Mat.All" "MaxLenInt" "
    ↪ Silicon" "PolySi" 0.5 1.4)
(sdedr:define-refinement-function "RefDef.Mat.All" "MaxLenInt" "
    ↪ Silicon" "Silicon" 0.5 1.4)

; Mesh the device
(sde:build-mesh "n1")

(system:command "svisual n1_msh.tdr &")
```

Analytic doping profiles

```
; Initialise workspace
(sde:clear)

; Create substrate doped regions
(sdegeo:create-rectangle (position 0 0 0) (position -4 -12 0) "
    ↪ Silicon" "Substrate_1")
(sdegeo:create-polygon (list
       (position -7 -6.6 0)
       (position -7 -8.4 0)
       (position -10 -8.4 0)
       (position -10 -7.2 0)
       (position -8.5 -7.2 0)
       (position -8.5 -6.6 0)
       (position -7 -6.6 0)
       )
       "Silicon"
       "Substrate_2"
)

; Create process doped regions
(sdegeo:create-rectangle (position -4 0 0) (position -7 -12 0) "
    ↪ Silicon" "DNW")
(sdegeo:create-rectangle (position -7 0 0) (position -8.5 -6.6 0) "
    ↪ Silicon" "NW_1")
(sdegeo:create-rectangle (position -7 -8.4 0) (position -8.5 -12 0) "
    ↪ Silicon" "NW_2.1")
(sdegeo:create-rectangle (position -8.5 -8.4 0) (position -10 -9 0) "
    ↪ Silicon" "NW_2.2")
(sdegeo:create-rectangle (position -8.5 -11.4 0) (position -10 -12 0)
    ↪  "Silicon" "NW_2.3")
```

```
(sdegeo:create-rectangle (position -8.5 -9 0) (position -10 -11.4 0)
    ↪ "PolySi" "NP")
(sdegeo:create-rectangle (position -8.5 0 0) (position -10 -7.2 0) "
    ↪ PolySi" "PP")

; Set oxide regions for insulation
(sdegeo:create-rectangle (position -10 -12 0) (position -11 -10.8 0)
    ↪ "Oxide" "Ox")
(sdegeo:create-rectangle (position -10 -9.6 0) (position -11 -6 0) "
    ↪ Oxide" "Ox")

; Define contacts for simulation
(sdegeo:set-contact (find-edge-id (position -10 -2 0)) "anode")
(sdegeo:set-contact (find-edge-id (position -10 -10.2 0)) "cathode")
(sdegeo:set-contact (find-face-id (position 0 2 0)) "bulk")

; Create a sweeping path and sweep along it
(define rectangular_path (sdegeo:create-polyline-wire (list
       (position 0 -6 0)
       (position 0 -6 2.5)
       (position 0 -2.5 6)
       (position 0 2.5 6)
       (position 0 6 2.5)
       (position 0 6 -2.5)
       (position 0 2.5 -6)
       (position 0 -2.5 -6)
       (position 0 -6 -2.5)
       (position 0 -6 0)
)))
(sdegeo:sweep (entity:faces (find-material-id "PolySi"))
    ↪ rectangular_path
  (sweep:options "solid" #t "rigid" #f "miter_type" "default" ))
(sdegeo:sweep (entity:faces (find-material-id "Silicon"))
    ↪ rectangular_path
  (sweep:options "solid" #t "rigid" #f "miter_type" "default" ))
(sdegeo:sweep (entity:faces (find-material-id "Oxide"))
    ↪ rectangular_path
  (sweep:options "solid" #t "rigid" #f "miter_type" "default" ))

; Define contacts for simulation
(sdegeo:set-contact (find-face-id (position -10 -2 0)) "anode")
(sdegeo:set-contact (find-face-id (position -10 2 0)) "anode")
(sdegeo:set-contact (find-face-id (position -10 0 -2)) "anode")
(sdegeo:set-contact (find-face-id (position -10 0 2)) "anode")
(sdegeo:set-contact (find-face-id (position 0 -2 0)) "bulk")
```

```
(sdegeo:set-contact (find-face-id (position 0 -2 2)) "bulk")
(sdegeo:set-contact (find-face-id (position 0 -2 -2)) "bulk")
(sdegeo:set-contact (find-face-id (position 0 0 -2)) "bulk")
(sdegeo:set-contact (find-face-id (position 0 2 -2)) "bulk")
(sdegeo:set-contact (find-face-id (position 0 -2 -2)) "bulk")
(sdegeo:set-contact (find-face-id (position 0 2 0)) "bulk")
(sdegeo:set-contact (find-face-id (position 0 2 2)) "bulk")
(sdegeo:set-contact (find-face-id (position 0 0 2)) "bulk")

; Define and set doping profiles
(sdedr:define-constant-profile "Substrate_doping" "
    ↪ BoronActiveConcentration" 1e+15)

(sdedr:define-constant-profile-region "Substrate_1_doping" "
    ↪ Substrate_doping" "Substrate_1")
(sdedr:define-constant-profile-region "Substrate_2_doping" "
    ↪ Substrate_doping" "Substrate_2")
(sdedr:define-constant-profile-region "DNW_base" "Substrate_doping" "
    ↪ DNW")
(sdedr:define-constant-profile-region "NW_1_base" "Substrate_doping"
    ↪ "NW_1")
(sdedr:define-constant-profile-region "NW_2.1_base" "Substrate_doping
    ↪ " "NW_2.1")
(sdedr:define-constant-profile-region "NW_2.2_base" "Substrate_doping
    ↪ " "NW_2.2")
(sdedr:define-constant-profile-region "NW_2.3_base" "Substrate_doping
    ↪ " "NW_2.3")
(sdedr:define-constant-profile-region "NP_base" "Substrate_doping" "
    ↪ NP")
(sdedr:define-constant-profile-region "PP_base" "Substrate_doping" "
    ↪ PP")

; Set BaseLine definitions for analytical profiles
(sdedr:define-refeval-window "BaseLine.DNW" "Polygon" (list
       (position -7 -11.8 -4.8)
       (position -7 -4.8 -11.8)
       (position -7 4.8 -11.8)
       (position -7 11.8 -4.8)
       (position -7 11.8 4.8)
       (position -7 4.8 11.8)
       (position -7 -4.8 11.8)
       (position -7 -11.8 4.8)
))
(sdedr:define-refeval-window "BaseLine.NW_1" "Polygon" (list
       (position -10 -6.2 -2.7)
```

```
        (position -10 -2.7 -6.2)
        (position -10 2.7 -6.2)
        (position -10 6.2 -2.7)
        (position -10 6.2 2.7)
        (position -10 2.7 6.2)
        (position -10 -2.7 6.2)
        (position -10 -6.2 2.7)
))
(sdedr:define-refeval-window "BaseLine.NW_2" "Polygon" (list
        (position -10 -11.8 -4.8)
        (position -10 -4.8 -11.8)
        (position -10 4.8 -11.8)
        (position -10 11.8 -4.8)
        (position -10 11.8 4.8)
        (position -10 4.8 11.8)
        (position -10 -4.8 11.8)
        (position -10 -11.8 4.8)
        (position -10 -11.8 -4.79)
        (position -10 -8.6 -3.71)
        (position -10 -8.6 3.7)
        (position -10 -3.7 8.6)
        (position -10 3.7 8.6)
        (position -10 8.6 3.7)
        (position -10 8.6 -3.7)
        (position -10 3.7 -8.6)
        (position -10 -3.7 -8.6)
        (position -10 -8.6 -3.7)
))
(sdedr:define-refeval-window "BaseLine.NP" "Polygon" (list
        (position -10 -11.2 -4.5)
        (position -10 -4.5 -11.2)
        (position -10 4.5 -11.2)
        (position -10 11.2 -4.5)
        (position -10 11.2 4.5)
        (position -10 4.5 11.2)
        (position -10 -4.5 11.2)
        (position -10 -11.2 4.5)
        (position -10 -11.2 -4.79)
        (position -10 -9.2 -3.91)
        (position -10 -9.2 3.9)
        (position -10 -3.9 9.2)
        (position -10 3.9 9.2)
        (position -10 9.2 3.9)
        (position -10 9.2 -3.9)
        (position -10 3.9 -9.2)
```

```
       (position -10 -3.9 -9.2)
       (position -10 -9.2 -3.9)
))
(sedr:define-refeval-window "BaseLine.PP" "Polygon" (list
       (position -10 -7 -2.8)
       (position -10 -2.8 -7)
       (position -10 2.8 -7)
       (position -10 7 -2.8)
       (position -10 7 2.8)
       (position -10 2.8 7)
       (position -10 -2.8 7)
       (position -10 -7 2.8)
))

; Define analytical doping profiles
(sedr:define-gaussian-profile "Gauss.DNW"
       "PhosphorusActiveConcentration" "PeakPos" 1.5 "PeakVal" 7.5
           ↪ e19
       "ValueAtDepth" 3e10 "Depth" 2.5 "Gauss" "Factor" 0.5)
(sedr:define-gaussian-profile "Gauss.NW_1"
       "PhosphorusActiveConcentration" "PeakPos" 1.5 "PeakVal" 1e16
       "ValueAtDepth" 3e14 "Depth" 0.4 "Gauss" "Factor" 0.5)
(sedr:define-gaussian-profile "Gauss.NW_2"
       "PhosphorusActiveConcentration" "PeakPos" 1.5 "PeakVal" 1e16
       "ValueAtDepth" 3e14 "Depth" 0.4 "Gauss" "Factor" 0.5)
(sedr:define-gaussian-profile "Gauss.NP"
       "PhosphorusActiveConcentration" "PeakPos" 0 "PeakVal" 5e21
       "ValueAtDepth" 3e19 "Depth" 0.7 "Gauss" "Factor" 0.2)
(sedr:define-gaussian-profile "Gauss.PP"
       "BoronActiveConcentration" "PeakPos" 0 "PeakVal" 5e21
       "ValueAtDepth" 3e19 "Depth" 0.7 "Gauss" "Factor" 0.3)

; Set analytical doping profiles
(sedr:define-analytical-profile-placement "PlaceAP.DNW"
       "Gauss.DNW" "BaseLine.DNW" "Positive" "Replace" "Eval")
(sedr:define-analytical-profile-placement "PlaceAP.NW_1"
       "Gauss.NW_1" "BaseLine.NW_1" "Positive" "NoReplace" "Eval")
(sedr:define-analytical-profile-placement "PlaceAP.NW_2"
       "Gauss.NW_2" "BaseLine.NW_2" "Positive" "NoReplace" "Eval")
(sedr:define-analytical-profile-placement "PlaceAP.NP"
       "Gauss.NP" "BaseLine.NP" "Positive" "NoReplace" "Eval")
(sedr:define-analytical-profile-placement "PlaceAP.PP"
       "Gauss.PP" "BaseLine.PP" "Positive" "NoReplace" "Eval")

; Define meshing strategy
```

```
(sdedr:define-refinement-size "RefDef.Mat.All" 10 10 10 0.5 0.5 0.5)
(sdedr:define-refinement-placement "Ref.Mat.All" "RefDef.Mat.All" (
    ↪ list "material" "Silicon" "material" "PolySi"))
(sdedr:define-refinement-function "RefDef.Mat.All" "
    ↪ DopingConcentration" "MaxTransDiff" 0.05)
(sdedr:define-refinement-function "RefDef.Mat.All" "MaxLenInt" "
    ↪ Silicon" "PolySi" 1 1.4)
(sdedr:define-refinement-function "RefDef.Mat.All" "MaxLenInt" "
    ↪ Silicon" "Silicon" 1 1.4)

; Mesh the device
(sde:build-mesh "n1")

(system:command "svisual n1_msh.tdr &")
```

Analytic doping profiles with STI declaration

Note that when compared to the standard analytic profile the material of `Substrate_2` block is changed to `Oxide` and the doping profile assignments are removed.

```
; Initialise workspace
(sde:clear)

; Create substrate doped regions
(sdegeo:create-rectangle (position 0 0 0) (position -4 -12 0) "
    ↪ Silicon" "Substrate_1")
(sdegeo:create-polygon (list
        (position -7 -6.6 0)
        (position -7 -8.4 0)
        (position -10 -8.4 0)
        (position -10 -7.2 0)
        (position -8.5 -7.2 0)
        (position -8.5 -6.6 0)
        (position -7 -6.6 0)
        )
        "Oxide"
        "Substrate_2"
)

; Create process doped regions
(sdegeo:create-rectangle (position -4 0 0) (position -7 -12 0) "
    ↪ Silicon" "DNW")
(sdegeo:create-rectangle (position -7 0 0) (position -8.5 -6.6 0) "
    ↪ Silicon" "NW_1")
(sdegeo:create-rectangle (position -7 -8.4 0) (position -8.5 -12 0) "
    ↪ Silicon" "NW_2.1")
(sdegeo:create-rectangle (position -8.5 -8.4 0) (position -10 -9 0) "
```

```
    ↪ Silicon" "NW_2.2")
(sdegeo:create-rectangle (position -8.5 -11.4 0) (position -10 -12 0)
    ↪  "Silicon" "NW_2.3")
(sdegeo:create-rectangle (position -8.5 -9 0) (position -10 -11.4 0)
    ↪ "PolySi" "NP")
(sdegeo:create-rectangle (position -8.5 0 0) (position -10 -7.2 0) "
    ↪ PolySi" "PP")

; Set oxide regions for insulation
(sdegeo:create-rectangle (position -10 -12 0) (position -11 -10.8 0)
    ↪ "Oxide" "Ox")
(sdegeo:create-rectangle (position -10 -9.6 0) (position -11 -6 0) "
    ↪ Oxide" "Ox")

; Define contacts for simulation
(sdegeo:set-contact (find-edge-id (position -10 -2 0)) "anode")
(sdegeo:set-contact (find-edge-id (position -10 -10.2 0)) "cathode")
(sdegeo:set-contact (find-face-id (position 0 2 0)) "bulk")

; Create a sweeping path and sweep along it
(define rectangular_path (sdegeo:create-polyline-wire (list
        (position 0 -6 0)
        (position 0 -6 2.5)
        (position 0 -2.5 6)
        (position 0 2.5 6)
        (position 0 6 2.5)
        (position 0 6 -2.5)
        (position 0 2.5 -6)
        (position 0 -2.5 -6)
        (position 0 -6 -2.5)
        (position 0 -6 0)
)))
(sdegeo:sweep (entity:faces (find-material-id "PolySi"))
    ↪ rectangular_path
  (sweep:options "solid" #t "rigid" #f "miter_type" "default" ))
(sdegeo:sweep (entity:faces (find-material-id "Silicon"))
    ↪ rectangular_path
  (sweep:options "solid" #t "rigid" #f "miter_type" "default" ))
(sdegeo:sweep (entity:faces (find-material-id "Oxide"))
    ↪ rectangular_path
  (sweep:options "solid" #t "rigid" #f "miter_type" "default" ))

; Define contacts for simulation
(sdegeo:set-contact (find-face-id (position -10 -2 0)) "anode")
(sdegeo:set-contact (find-face-id (position -10 2 0)) "anode")
```

```
(sdegeo:set-contact (find-face-id (position -10 0 -2)) "anode")
(sdegeo:set-contact (find-face-id (position -10 0 2)) "anode")
(sdegeo:set-contact (find-face-id (position 0 -2 0)) "bulk")
(sdegeo:set-contact (find-face-id (position 0 -2 2)) "bulk")
(sdegeo:set-contact (find-face-id (position 0 -2 -2)) "bulk")
(sdegeo:set-contact (find-face-id (position 0 0 -2)) "bulk")
(sdegeo:set-contact (find-face-id (position 0 2 -2)) "bulk")
(sdegeo:set-contact (find-face-id (position 0 -2 -2)) "bulk")
(sdegeo:set-contact (find-face-id (position 0 2 0)) "bulk")
(sdegeo:set-contact (find-face-id (position 0 2 2)) "bulk")
(sdegeo:set-contact (find-face-id (position 0 0 2)) "bulk")

; Define and set doping profiles
(sdedr:define-constant-profile "Substrate_doping" "
    ↪ BoronActiveConcentration" 1e+15)

(sdedr:define-constant-profile-region "Substrate_1_doping" "
    ↪ Substrate_doping" "Substrate_1")
(sdedr:define-constant-profile-region "DNW_base" "Substrate_doping" "
    ↪ DNW")
(sdedr:define-constant-profile-region "NW_1_base" "Substrate_doping"
    ↪ "NW_1")
(sdedr:define-constant-profile-region "NW_2.1_base" "Substrate_doping
    ↪ " "NW_2.1")
(sdedr:define-constant-profile-region "NW_2.2_base" "Substrate_doping
    ↪ " "NW_2.2")
(sdedr:define-constant-profile-region "NW_2.3_base" "Substrate_doping
    ↪ " "NW_2.3")
(sdedr:define-constant-profile-region "NP_base" "Substrate_doping" "
    ↪ NP")
(sdedr:define-constant-profile-region "PP_base" "Substrate_doping" "
    ↪ PP")

; Set BaseLine definitions for analytical profiles
(sdedr:define-refeval-window "BaseLine.DNW" "Polygon" (list
       (position -7 -11.8 -4.8)
       (position -7 -4.8 -11.8)
       (position -7 4.8 -11.8)
       (position -7 11.8 -4.8)
       (position -7 11.8 4.8)
       (position -7 4.8 11.8)
       (position -7 -4.8 11.8)
       (position -7 -11.8 4.8)
))
(sdedr:define-refeval-window "BaseLine.NW_1" "Polygon" (list
```

```
        (position -10 -6.2 -2.7)
        (position -10 -2.7 -6.2)
        (position -10 2.7 -6.2)
        (position -10 6.2 -2.7)
        (position -10 6.2 2.7)
        (position -10 2.7 6.2)
        (position -10 -2.7 6.2)
        (position -10 -6.2 2.7)
))
(sdedr:define-refeval-window "BaseLine.NW_2" "Polygon" (list
        (position -10 -11.8 -4.8)
        (position -10 -4.8 -11.8)
        (position -10 4.8 -11.8)
        (position -10 11.8 -4.8)
        (position -10 11.8 4.8)
        (position -10 4.8 11.8)
        (position -10 -4.8 11.8)
        (position -10 -11.8 4.8)
        (position -10 -11.8 -4.79)
        (position -10 -8.6 -3.71)
        (position -10 -8.6 3.7)
        (position -10 -3.7 8.6)
        (position -10 3.7 8.6)
        (position -10 8.6 3.7)
        (position -10 8.6 -3.7)
        (position -10 3.7 -8.6)
        (position -10 -3.7 -8.6)
        (position -10 -8.6 -3.7)
))
(sdedr:define-refeval-window "BaseLine.NP" "Polygon" (list
        (position -10 -11.2 -4.5)
        (position -10 -4.5 -11.2)
        (position -10 4.5 -11.2)
        (position -10 11.2 -4.5)
        (position -10 11.2 4.5)
        (position -10 4.5 11.2)
        (position -10 -4.5 11.2)
        (position -10 -11.2 4.5)
        (position -10 -11.2 -4.79)
        (position -10 -9.2 -3.91)
        (position -10 -9.2 3.9)
        (position -10 -3.9 9.2)
        (position -10 3.9 9.2)
        (position -10 9.2 3.9)
        (position -10 9.2 -3.9)
```

```
        (position -10 3.9 -9.2)
        (position -10 -3.9 -9.2)
        (position -10 -9.2 -3.9)
))
(sdedr:define-refeval-window "BaseLine.PP" "Polygon" (list
        (position -10 -7 -2.8)
        (position -10 -2.8 -7)
        (position -10 2.8 -7)
        (position -10 7 -2.8)
        (position -10 7 2.8)
        (position -10 2.8 7)
        (position -10 -2.8 7)
        (position -10 -7 2.8)
))

; Define analytical doping profiles
(sdedr:define-gaussian-profile "Gauss.DNW"
        "PhosphorusActiveConcentration" "PeakPos" 1.5 "PeakVal" 7.5
            ↪ e19
        "ValueAtDepth" 3e10 "Depth" 2.5 "Gauss" "Factor" 0.5)
(sdedr:define-gaussian-profile "Gauss.NW_1"
        "PhosphorusActiveConcentration" "PeakPos" 1.5 "PeakVal" 1e16
        "ValueAtDepth" 3e14 "Depth" 0.4 "Gauss" "Factor" 0.5)
(sdedr:define-gaussian-profile "Gauss.NW_2"
        "PhosphorusActiveConcentration" "PeakPos" 1.5 "PeakVal" 1e16
        "ValueAtDepth" 3e14 "Depth" 0.4 "Gauss" "Factor" 0.5)
(sdedr:define-gaussian-profile "Gauss.NP"
        "PhosphorusActiveConcentration" "PeakPos" 0 "PeakVal" 5e21
        "ValueAtDepth" 3e19 "Depth" 0.7 "Gauss" "Factor" 0.2)
(sdedr:define-gaussian-profile "Gauss.PP"
        "BoronActiveConcentration" "PeakPos" 0 "PeakVal" 5e21
        "ValueAtDepth" 3e19 "Depth" 0.7 "Gauss" "Factor" 0.3)

; Set analytical doping profiles
(sdedr:define-analytical-profile-placement "PlaceAP.DNW"
        "Gauss.DNW" "BaseLine.DNW" "Positive" "NoReplace" "Eval")
(sdedr:define-analytical-profile-placement "PlaceAP.NW_1"
        "Gauss.NW_1" "BaseLine.NW_1" "Positive" "NoReplace" "Eval")
(sdedr:define-analytical-profile-placement "PlaceAP.NW_2"
        "Gauss.NW_2" "BaseLine.NW_2" "Positive" "NoReplace" "Eval")
(sdedr:define-analytical-profile-placement "PlaceAP.NP"
        "Gauss.NP" "BaseLine.NP" "Positive" "NoReplace" "Eval")
(sdedr:define-analytical-profile-placement "PlaceAP.PP"
        "Gauss.PP" "BaseLine.PP" "Positive" "NoReplace" "Eval")
```

```
; Define meshing strategy
(sdedr:define-refinement-size "RefDef.Mat.All" 10 10 10 0.5 0.5 0.5)
(sdedr:define-refinement-placement "Ref.Mat.All" "RefDef.Mat.All" (
    ↪ list "material" "Silicon" "material" "PolySi"))
(sdedr:define-refinement-function "RefDef.Mat.All" "
    ↪ DopingConcentration" "MaxTransDiff" 0.05)
(sdedr:define-refinement-function "RefDef.Mat.All" "MaxLenInt" "
    ↪ Silicon" "PolySi" 1 1.4)
(sdedr:define-refinement-function "RefDef.Mat.All" "MaxLenInt" "
    ↪ Silicon" "Silicon" 1 1.4)

; Mesh the device
(sde:build-mesh "n1")

(system:command "svisual n1_msh.tdr &")
```

B.2. SENTAURUS DEVICE COMMAND FILES

B.2.1. I-V SIMULATION

```
File{
        Grid  = "n1_msh.tdr"
        Plot  = "n2_des.tdr"
        Current  = "n2_des.plt"
        Output  = "n2_des.log"
}

Electrode{
        { Name="anode"  Voltage=0.0 }
        { Name="cathode" Voltage=0.0 }
        { Name="bulk"  Voltage=0.0 } * also seen as the substrate
}

Physics{
        Fermi
        EffectiveIntrinsicDensity( BandGapNarrowing(OldSlotboom) )
        Mobility(
                DopingDep
                eHighFieldsaturation( GradQuasiFermi )
                hHighFieldsaturation( GradQuasiFermi )
                Enormal
        )
        Recombination(
                SRH( DopingDependence )
                Avalanche( vanOverstraeten ElectricField )
```

```
        )
}

Plot{
        *--Density and Currents, etc
        eDensity hDensity
        TotalCurrent/Vector eCurrent/Vector hCurrent/Vector
        eMobility/Element hMobility/Element
        eVelocity hVelocity
        eQuasiFermi hQuasiFermi

        *--Temperature
        eTemperature hTemperature Temperature

        *--Fields and charges
        ElectricField/Vector Potential SpaceCharge

        *--Doping Profiles
        Doping DonorConcentration AcceptorConcentration

        *--Generation/Recombination
        SRH Band2Band Auger
        ImpactIonization eImpactIonization hImpactIonization

        *--Driving forces
        eGradQuasiFermi/Vector hGradQuasiFermi/Vector
        eEparallel hEparallel eENormal hENormal

        *--Band structure/Composition
        BandGap
        BandGapNarrowing
        Affinity
        ConductionBand ValenceBand
        eQuantumPotential hQuantumPotential
}

Math{
        RefDens_eGradQuasiFermi_ElectricField_HFS = 1e12
        RefDens_hGradQuasiFermi_ElectricField_HFS = 1e12

        Extrapolate
        ExtendedPrecision
        NumberOfThreads=Maximum

        Derivatives
```

```
        Avalderivatives

        RelErrControl
        Digits=4

        Iterations=50
        NotDamped=100

        BreakCriteria{ Current(Contact="cathode" AbsVal=1e-6) }
}

Solve{
    * initial solution
        NewCurrentPrefix="init_"
        Coupled(Iterations=100){ Poisson eQuantumPotential }
        Coupled { Poisson Electron Hole eQuantumPotential }

        Save ( FilePrefix = "n2_init" )

    * final simulatin to find the I-V curve
        NewCurrentPrefix="IV_"
        Quasistationary(
                InitialStep=0.1e-3 Increment=2 Decrement=1 MinStep=1e
                    ↪ -15 MaxStep=0.5
                Goal { Name="cathode" Voltage=40 }
        ) { Coupled { Poisson Electron Hole eQuantumPotential }
                *Plot the device structure at given time intervals for
                    ↪  verification of internal fields
                Plot( -Loadable Fileprefix="n2_inter_" NoOverWrite
                    ↪ Time= (0.1; 0.2; 0.3; 0.4; 0.5; 0.6; 0.7; 0.8;
                    ↪ 0.9; 1.0) )
                *I-V calculated at regular intervals
                CurrentPlot(Time=(Range=(0 1) Intervals=200))
        }


}
```

B.2.2. C-V SIMULATION

```
* define the model as a circuit device
Device "SPAD"{
File{
        Grid  = "n1_msh.tdr"
        Plot  = "n3_des.tdr"
```

```
        Current  = "n3_des.plt"
}

Electrode{
        { Name="anode"  Voltage=0.0 }
        { Name="cathode" Voltage=0.0 }
        { Name="bulk"  Voltage=0.0 } * also seen as the substrate
}

Physics{
        Fermi
        EffectiveIntrinsicDensity( BandGapNarrowing(OldSlotboom) )
        Mobility(
                DopingDep
                eHighFieldsaturation( GradQuasiFermi )
                hHighFieldsaturation( GradQuasiFermi )
                Enormal
        )
        Recombination(
                SRH( DopingDependence )
                Avalanche( ElectricField )
        )
}
} * End of SPAD device

Plot{
        *--Density and Currents, etc
        eDensity hDensity
        TotalCurrent/Vector eCurrent/Vector hCurrent/Vector
        eMobility/Element hMobility/Element
        eVelocity hVelocity
        eQuasiFermi hQuasiFermi

        *--Temperature
        eTemperature hTemperature Temperature

        *--Fields and charges
        ElectricField/Vector Potential SpaceCharge

        *--Doping Profiles
        Doping DonorConcentration AcceptorConcentration

        *--Generation/Recombination
        SRH Band2Band Auger
        ImpactIonization eImpactIonization hImpactIonization
```

```
        *--Driving forces
        eGradQuasiFermi/Vector hGradQuasiFermi/Vector
        eEparallel hEparallel eENormal hENormal

        *--Band structure/Composition
        BandGap
        BandGapNarrowing
        Affinity
        ConductionBand ValenceBand
        eQuantumPotential hQuantumPotential
}

Math{
        RefDens_eGradQuasiFermi_ElectricField_HFS = 1e12
        RefDens_hGradQuasiFermi_ElectricField_HFS = 1e12

        Extrapolate
        ExtendedPrecision
        NumberOfThreads=Maximum

        Derivatives
        Avalderivatives

        RelErrControl
        Digits=4

        Iterations=50
        NotDamped=100

}

File{
        Output = "simCV_des.log"
}

* circuit netlist
System {
        SPAD SPAD1 ( "cathode" = cat "anode" = an "bulk" = bulk)

        Vsource_pset vc (cat 0){dc=0}
        Vsource_pset va (an 0){dc=0}
        Vsource_pset vbulk (bulk 0){dc=0}
}
```

```
Solve {
        * initial solution
        NewCurrentPrefix="init_"
        Coupled(Iterations=100){ Poisson eQuantumPotential }
        Coupled { Poisson Electron Hole eQuantumPotential }

        Save ( FilePrefix = "n2_init" )

    * final simulation to find the C-V curve
        NewCurrentPrefix="CV_"

        Quasistationary(
                InitialStep=0.1e-3 Increment=2 MinStep=1e-15 MaxStep
                    ↪ =0.5
                Goal { Parameter=vc.dc Voltage=40 }
        )
        { ACCoupled (
                StartFrequency=1e4 EndFrequency=1e6
                NumberOfPoints=20 Decade
                Node(cat an bulk) Exclude(vc va vbulk)
                )
                { Poisson Electron Hole eQuantumPotential }
        }
}
```

C
APPENDIX C - FURTHER INFORMATION

C.1. CMOS MANUFACTURING PROCESSES AND ASSUMPTIONS MADE

The designed layout of the SPAD by [28] has been and the Integration and Optimization group will be manufactured by TSMC using their 40nm CMOS node. This CMOS process consists of multiple lithography steps such as etching, deposition, and implantation. The exact description of this process was not available to us, so we had no ability to simulate the process one-to-one.

Alternatively, it is possible to make an educated guess on the final device structure and doping profiles. The device structure will be directly based upon the cross-sectional designs seen in Fig. 3.1 and their correspondent symmetries. To make an educated guess for the doping profiles there were two options: constant doping profiles and profiles based upon analytic functions. Both of these options were taken into account to show an ideal situation and one that more reflects the final device.

For the latter option, it was assumed that the concentration of dopant atoms followed a gaussian retrograde profile, characteristic to ion implantation [31]. Because of the fact that we are able to assume the implantation depths, the implantation energies were not explicitly assumed, but it was assumed that the Deep N-well has a higher implantation energy than the N-well, which in turn has a higher implantation energy than the N+ and P+ regions. Therefore creating the desired device structure.

To finalise the educated guess on the doping profiles, the doping concentrations had to be guessed. Several different options were tried, but the most promising one consisted of a P substrate and N-well doping concentration in the order of 10^{15}cm^{-3}, a DNW doping concentration in the order of 10^{19}cm^{-3}, and a P+ and N+ doping concentration in the order of 10^{21}cm^{-3}. These are the same for both the constant doping profiles and the analytic profiles, with the exception for the N-well where the peak concentration was made to be $1 \cdot 10^{16}\text{cm}^{-3}$ to account for the retrograde profile.